

Nonlinear response of a quantum cascade laser in a high intensity electromagnetic field

David Winge

Supervisor: Andreas Wacker

Division of Mathematical Physics, Lund University

June 12, 2012

Abstract

A theoretical study is presented, in which the *nonlinear response* of a biased Quantum Cascade Laser (QCL) is calculated. The calculations are based on the *nonequilibrium Green's function* formalism. Assuming a periodic electromagnetic field in the calculations, this formalism provides not only the stationary behavior Green's functions, but also the part of the response that varies in time according to the oscillating electromagnetic field.

In this work the *Fourier components* of the response are calculated, and the dynamics of the system is thus expressed in a Fourier series with the fundamental response and its *higher harmonics*. By including at first only the fundamental and the most prominent harmonics, the ones of low order, we can then increase the accuracy of the method by including even higher harmonics, needed for high intensity calculations.

The calculations are done on a four well resonant-phonon QCL that has been studied by Burghoff *et al*, Applied Physics Letters **98**, 061112 (2011), where the gain of the structure was successfully measured. In this work the findings of the simulations are compared to their measurements to find that the high intensity calculations of the nonlinear response agree best with the experimental data. This suggests that the intensity used in the experimental measurements do not correspond to linear response.

By relating the response of the system at different biases and external light field intensities, a theoretical connection to *gain clamping* could also be established, and the output power approaching the operating point calculated and related with good agreement to experiment. In addition, the integrated absorption is calculated, and the relevance of electron-electron scattering and convergence issues are addressed.

Contents

1	Quantum Cascade Lasers	4
1.1	IR-QCLs and THz-QCLs	4
1.2	Basic principle	4
1.3	QCL designs	5
1.3.1	Depopulation of the lower laser state	6
1.3.2	Increasing the lifetime of the upper laser state	6
1.3.3	Waveguide	7
1.4	Physics of a QCL	7
1.5	Gain in a high intensity system	8
2	Theory	10
2.1	Equilibrium Green's function	10
2.1.1	Pictures	10
2.1.2	History and future	12
2.1.3	Wick's theorem	13
2.1.4	Example Hamiltonian	13
2.1.5	Self consistent Born approximation	16
2.1.6	Eq. of motion for the Green's function	16
2.2	Non-Equilibrium Green's functions	17
2.2.1	Contour ordering	17
2.2.2	Langreth theorem	18
2.2.3	The equations of motion in real time	18
2.3	Translational invariance and the Fourier transforms	19
2.3.1	Self energies Σ	21
2.3.2	Mean field potential	23
2.3.3	EM-field in Lorenz gauge	23
2.4	A simple model of gain between subband states	24
2.4.1	Modal gain	24
2.5	Integrated absorption	26
2.5.1	Thomas Reiche Kuhn sum rule [1][2]	26
2.5.2	Subband absorption	27
2.6	Basis States	27
2.6.1	Wannier States	28
2.6.2	Wannier-Stark states	28
2.7	Gain calculated with the Green's functions	28
3	Results	30
3.1	Reference results	30
3.2	Description and classification of the QCL	32
3.3	Interface Roughness Scattering Parameter	33
3.4	Linear response of a QCL	35
3.4.1	Linear response calculations	35
3.4.2	Identifying energy transitions	36
3.4.3	Densities and Spectral functions & Red and Blue shift of transitions	38

3.4.4	Modal gain calculations	40
3.4.5	Rediagonalizing the density matrix	41
3.5	Nonlinear response calculations	44
3.5.1	Gain clamping	46
3.5.2	Convergence studies	48
3.6	Energy shifted peaks in gain spectra	50
3.7	Integrated absorption of a QCL	53
3.8	Phenomenological inclusion of electron-electron scattering	55
4	Conclusion	57

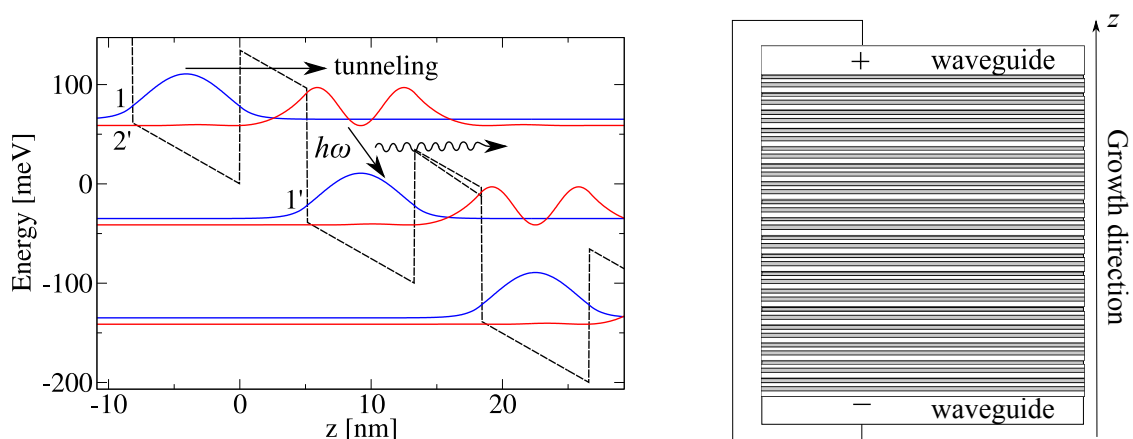
1 Quantum Cascade Lasers

A quantum cascade laser (QCL) is a layered heterostructure encapsulated in a waveguide supporting chosen wavelengths. They make use of the subbands of semiconductors, and by design and an external bias over the structure population inversion among the states are achieved. This means that states of higher energy are more occupied than lower lying state, on the contrary to the normal situation.

1.1 IR-QCLs and THz-QCLs

Depending on in which region of the optical spectra QCLs operate, they are often called different names. Laser of relative high energy operate in what is called the “mid-IR”, around 3-15 μm (80-400 meV). At lower energies we find “far-IR-QCLs”, 15-100 μm (15-80 meV), and at last “THz-QCLs” operating at 0.1-1 mm (1-15 meV). As the thermal energy of an electron is ≈ 25 meV, building QCLs in the THz regime is a big technical challenge. Especially as many designs have layer thicknesses as small as 0.5 nm.

1.2 Basic principle



(a) The basic idea of an QCL (although this is not a working laser!). The heterostructure is biased so it has a tilted shape. For each sequence a photon is emitted due to deexcitation necessary for transport. Each period in this superlattice consists of a 5.1 nm barrier and a 8.2 nm well.

(b) The QCL is built by layering semiconductors with different conduction band edges, creating the band potential structure in (a).

Figure 1

The periodic structure of a QCL has layers of different widths of different semiconductors stacked on top of each other, creating a structure of barriers and wells in the potential as seen in figures 1a and 1b. This will give rise to bound states as the movement of the electrons is quantized in the growth direction (usually denoted z) but exhibits a 'free' behavior in the other two directions, the *in-plane*-direction (in the usual case then x and y). Free as in seeing no potential difference in those

directions. In these directions the electron dispersion will be parabolic in k , providing a large degeneracy for the states quantized in z .

Electrons rippling down a structure as seen in fig. 1a would only give some light due to spontaneous emission, and this would surely be absorbed again in a later period, or in best of cases, generate an incoherent light source. To build a laser giving coherent light, one needs population inversion. If this is achieved, one spontaneous emission would be stimulated emission at each period double the intensity, and the light would be coherent. The design challenge is thus to create a semiconductor structure, capable of creating population inversion of states matching the energy difference $\hbar\omega$ of the desired laser light.

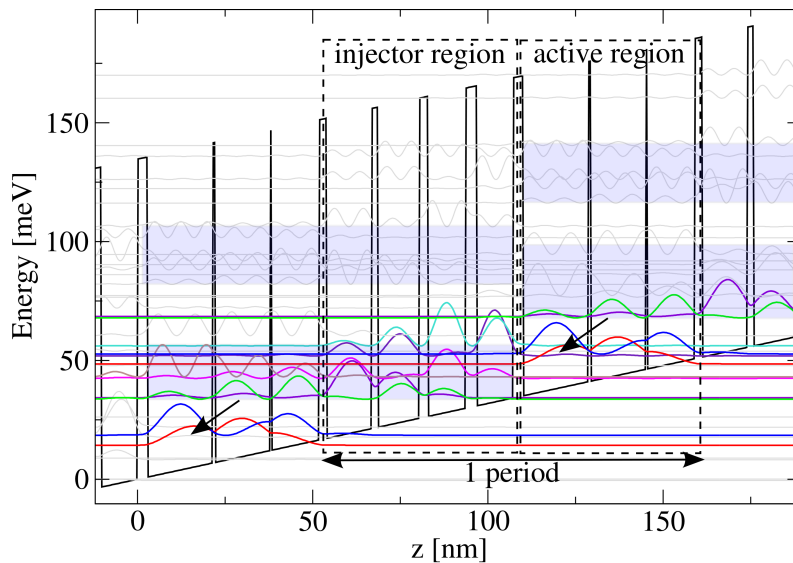


Figure 2: An example QCL based on a chirped superlattice design presented in Ref. [3] of $\text{Al}_{0.15}\text{Ga}_{0.85}\text{As}/\text{GaAs}$. The decomposition of one period is **3.0**/18.6/**0.7**/15.4/**0.5**/13.6/**2.3**/12.8/**1.8**/11.8/**2.3**/10.8/**3.2**/10.4 nm, where bold means barrier.

1.3 QCL designs

In this brief discussion we will not go into all of the details and all of the different designs that can be found in the literature [4][5]. Instead we will shortly introduce some central concepts and discuss a few different strategies for achieving population inversion. Some of them are of particular interest in this work.

In fig. 2 a chirped superlattice design is shown. The shaded regions show areas where there are many states to jump between. Here the electrons are expected to relax down to the lowest state. From here (green/indigo curve), there is no way to go but down to next group of states, where the electrons again relax, and the process repeats itself. In this design the population inversion is created by a quick deexcitation by phonons and electron-electron scattering through the 'blur of states' in the injector region, hopefully leaving the top state sparsely occupied, but the lowest at a high level of occupation.

Having introduced the active region - the part of the period where we have an

inverted population, the injector region - the part that transports and relaxes the electrons, and also empties the lower laser state, we proceed by discussing some more design strategies below.

1.3.1 Depopulation of the lower laser state

Quick extraction of electrons from the lower laser state is essential in order to establish population inversion. One popular method is the *resonant tunneling* extraction, and the idea is that by aligning a state in a neighboring well to the lower laser state, and making sure they have a decent overlap, electrons will tunnel through and thus leave the lower laser state. This process is then often followed by other transport and scattering processes. In fig. 2 the tunneling is followed by a smooth phonon/electron-electron deexcitation, in figs. 3a,3b this is done by optical phonon transitions¹. The latter is an efficient method for extracting electron for two reasons.

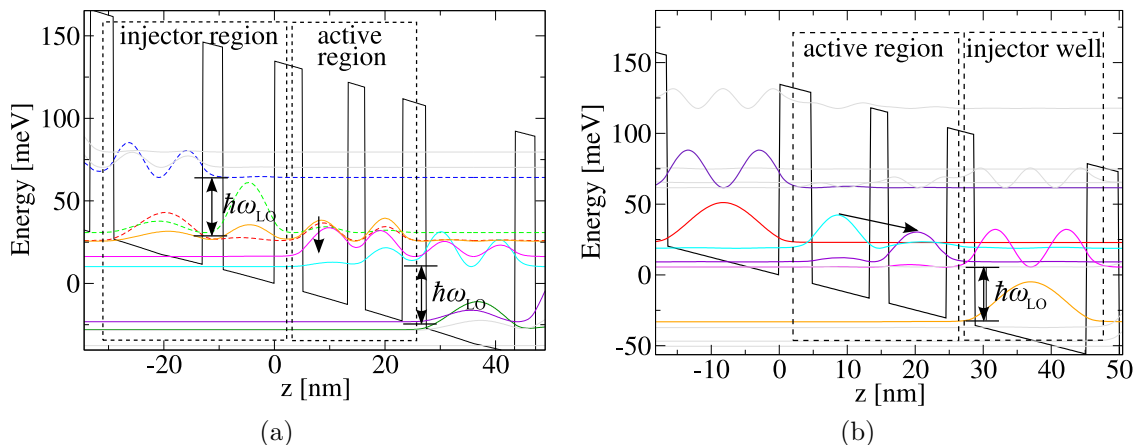


Figure 3: Examples of vertical [6] (a) and diagonal [7] (b) QCL design with resonant optical phonon extraction.

First of all, this method is quick, as the scattering rate of optical phonons is high. If the lower laser state can be positioned exactly one optical phonon energy over this state quick depopulation is ensured. Electrons taking this path will then be fed into the next injector region and hopefully fed correctly into the next active region, as seen in figs. 3a,3b. Another advantage is that the phonon transition is large in energy, compared to the laser energies of especially THz-QCLs. In GaAs systems, the longitudinal optical phonon energy is 36 meV, and the laser transition is usually between 10-15 meV. Comparing figs. 2 and 3 we can see that thermal excitations of the electrons are more likely to fill the lower laser state in fig 2 as the energy difference is smaller here. Although at room temperature, the optical phonon energy ($\hbar\omega_{LO}$) is not anymore large compared to the thermal energy, causing *thermal backfilling* also in the schemes of fig. 3.

¹An optical phonon is a quantized intramolecular vibrational mode possible in a crystal with more than one type of atom. in quantum mechanics this is often treated as a bosonic particle.

1.3.2 Increasing the lifetime of the upper laser state

A condition for stable inversion is that the electrons stay sufficiently long in the upper laser state to be deexcited by stimulated emission. Therefore it is important to design the lifetime of this state. Eq. (1) shows an expression for modal gain derived from Fermi's Golden Rule (derivation in sec. 2.4.1 following [8]). Gain is the opposite of absorption, it is the number of times the field is enhanced per unit length in the structure.

$$G(\omega) = \frac{e^2 |z_{lo,up}|^2 \omega (n_{up} - n_{low})}{2dc\epsilon_0 \sqrt{\epsilon_r}} \frac{\Gamma}{(E_{up} - E_{lo} - \hbar\omega)^2 + \Gamma^2/4} \quad (1)$$

$z_{lo,up}$ is the dipole matrix element, $n_{up/lo}$ is the density of the upper and lower levels respectively, d is the period length of the structure, Γ is a broadening i.e. the full width maximum which is dependent of the lifetime of the state considered, ω is the frequency and E is the energies for the different states.

From this equation we see that apart from inversion, it is also good to have a large matrix element, as this comes in squared in eq. 53. Vertical designs achieve this with a large overlap between the upper and lower laser state, as in fig. 3a, where a large overlap is created between the upper (orange) and lower (pink) laser state. Large overlaps however decrease the lifetime of the upper laser state, limiting inversion. The vertical designs have been very successful in the IR region, with QCL lasing at room temperature [9]. Diagonal designs are instead created to have smaller overlap in order to prolong the upper laser state lifetime, study fig. 3b where the upper (cyan) and lower (purple) laser state is now spatially separated by a barrier. As higher lifetimes seem to be more important than the matrix element at lower energy lasers, these designs have recently been successful in creating THz-QCL lasing at 186 K [7]. Designing a QCL is a game of balance between parameters such as lifetimes and overlap of states. (The overlap between states that are supposed to be in resonant tunneling with each other is also an important factor, and to make sure that the QCL operates in a positive differential conductance region.)

1.3.3 Waveguide

In order to achieve lasing in the QCL, the light has to be confined in order for stimulated emission and consequently intensity enhancement to occur. This is done by encapsulating the heterostructure in a waveguide. The waveguide, by its geometry, supports only certain wavelengths, although a QCL is capable of gain over a broader range of wavelength, as we shall see. Mainly two types of waveguides have been studied in the literature for THz-QCL, the semi-insulating surface-plasmon waveguide (SI-SP) and the metal-metal (MM) waveguide [4], and at the moment the MM waveguide beats the SI-SP at higher temperatures whereas the latter has better output power and beam structure.

1.4 Physics of a QCL

In order to approach these systems on a theoretical level, we have to know which physical effects to include. In a complete approach, the following has to be treated;

- the heterostructure potential and a bias over the system
- the quantized states and their limited lifetime due to scattering
- tunneling through barriers
- acoustic and optical phonons
- interface roughness scattering and alloy scattering
- electron-electron scattering/coulomb repulsion
- *interactions with an oscillating electromagnetic field

Here the last entrance has a star, due to the optionality; one can calculate the transport through a system without taking an external light field into account. Interface roughness is caused by the fact that when growing a QCL structure, the interfaces between different semiconductor materials are not entirely perfect. Some islands of monolayer thickness will create a potential difference scattering electrons. The alloy scattering comes from introducing other materials in a parent material, for example mixing Al in GaAs to get a new semiconductor with different CBO. The electrons will then scatter on the slightly different Al atoms in the alloy. Solving the transport problem for a system like this is complicated for a number of reasons. The solution is not an equilibrium, we cannot use any ordinary statistics as we seek a steady state solution that is indeed dynamic in its nature. Looking at high intensity phenomena, as in this work, it is necessary to treat the interactions of the steady state solution with an electromagnetic field also when these perturbations are not small.

A straight-forward approach is to use the density matrix approach together with rate equations to handle scattering. Lifetimes and other properties of the states can then be found self-consistently. Using that approach current is often well reproduced, but it is hard to extract observables other than the densities of that system. Using the Non Equilibrium Green's Function (NEGF) formalism, observables of high interest such as gain and energetical resolved densities can be found by a self consistent approach.

1.5 Gain in a high intensity system

Gain is the key physical property in a QCL. It is the fundamental thing that will decide the operating limits of a specific structure. To build a THz-QCL that lases at room temperatures, high gain must be supported even at these high temperatures. A big problem is that gain is neither easy to measure nor to simulate.

One of the main advantages of the NEGF-model used in this work is that gain is calculated. In addition, an article recently published [6] presents a method of measuring gain at high accuracy, and some of their results are presented in fig. 4. Now we have a model for calculating gain and an experiment measuring gain. Three questions arise.

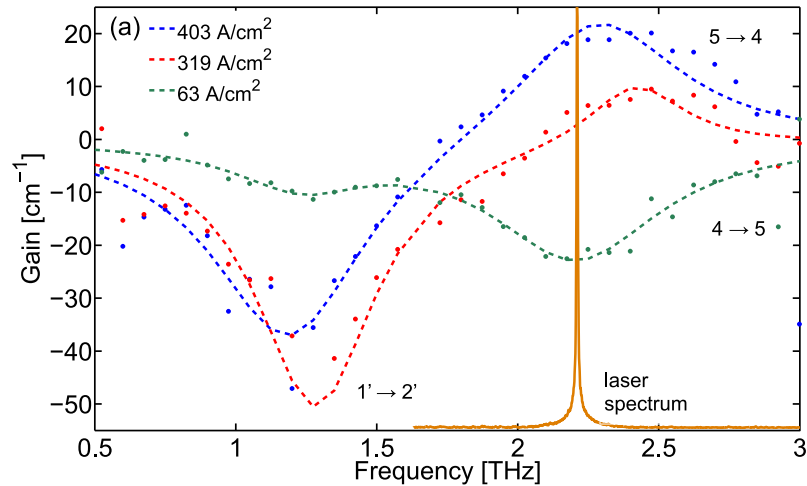


Figure 4: Gain measured by Burghoff *et al.* [6] for three different currents. The high current shows the gain spectra at operating conditions.

Can we reproduce the gain measurements in the experiment by simulations? This might give valuable insight in the model we use.

How can we interpret gain clamping in a theoretical picture? Gain clamping (a concept that will be thoroughly addressed later) occurs when the enhancement of light in a structure is more than the losses of the system, and the intensity at this point will be related to the output power of the structure. Can we approach these concepts theoretically?

What are the limits to our model when we go to high intensities? The optical power can be high in a QCL, and a strong laser field might give rise to nonlinear dynamics in the system. Experimentally this is of course no problem, but what are the limits when we look at this by a mathematical model?

2 Theory

In this section we recapitulate the main parts of the theoretical discussion in the literature leading to firstly, the equilibrium Green's function and its diagrammatic expansion, and secondly, the non equilibrium Green's function by contour integrals and analytic continuation. It is to be read as my view on the theoretical framework and not as an novice introduction. The reader not familiar with Green's functions, or readers very familiar to Green's functions might continue at section 2.3.

The first two parts of this section follow mostly H. Haug and A.-P Jauho (1996) with some details from M.E. Peskin and D.V. Schroeder (1995). For more details the reader is urged to consult [10][11].

2.1 Equilibrium Green's function

The equilibrium Green's function is defined as

$$G(\mathbf{x}, t, \mathbf{x}', t') = -\frac{i}{\hbar} \frac{\langle \Psi_0 | T \{ \psi_H(\mathbf{x}, t) \psi_H^\dagger(\mathbf{x}', t') \} | \Psi_0 \rangle}{\langle \Psi_0 | \Psi_0 \rangle}, \quad (2)$$

where Ψ_0 is the ground state, T is the fermionic time ordering operator and the H of the Ψ 's are referring to the Heisenberg picture. The time ordered operator for the two field operators is defined as:

$$T\{\psi(\mathbf{x}, t)\psi^\dagger(\mathbf{x}', t')\} = \theta(t - t')\psi(\mathbf{x}, t)\psi^\dagger(\mathbf{x}', t') - \theta(t' - t)\psi^\dagger(\mathbf{x}', t')\psi(\mathbf{x}, t),$$

where the minus sign comes from interchanging the two fermionic operators in the second term. For bosons, it would have been the other way.

2.1.1 Pictures

Now we turn to the state vectors Ψ . In Schrödinger picture we have, if the Hamiltonian H has no explicit time dependence,

$$\begin{aligned} i\hbar \frac{\partial}{\partial t} |\Psi_S(t)\rangle &= H |\Psi_S(t)\rangle \\ |\Psi_S(t)\rangle &= e^{-iH(t-t_0)/\hbar} |\Psi_S(t_0)\rangle \end{aligned}$$

where all time dependence is in the states. In Heisenberg picture we have instead

$$\begin{aligned} |\Psi_H(t)\rangle &\equiv e^{iHt/\hbar} |\Psi_S(t)\rangle \\ \Rightarrow \frac{\partial}{\partial t} |\Psi_H(t)\rangle &= 0 \\ O_H(t) &\equiv e^{iHt/\hbar} O_S e^{-iHt/\hbar} \end{aligned}$$

where the time dependence is in the operators, governed by the full Hamiltonian. In order to make a perturbative expansion, we split the Hamiltonian H into two parts, one 'simple' that we assume that we can solve and diagonalize, H_0 , and another, H^{int} that is 'harder' to solve and will be nondiagonal, containing for example interactions,

but that can be treated in a perturbative manner; $H = H_0 + H^{int}$. Now we define the interaction picture:

$$|\Psi_I(t)\rangle \equiv e^{iH_0t/\hbar}|\Psi_S(t)\rangle. \quad (3)$$

Here we notice that at $t = 0$, all three state vectors of the different pictures coincide. By differentiating, one finds

$$\begin{aligned} i\hbar \frac{\partial}{\partial t} |\Psi_I(t)\rangle &= H_I^{int}(t) |\Psi_I(t)\rangle \\ H_I^{int}(t) &= e^{iH_0t/\hbar} H^{int} e^{-iH_0t/\hbar} \\ (O_I^{int}(t) &= e^{iH_0t/\hbar} O_S^{int} e^{-iH_0t/\hbar}) \end{aligned} \quad (4)$$

and by differentiating again, one finds by using eq. (4)

$$i\hbar \frac{\partial}{\partial t} O_I(t) = [O_I(t), H_0]$$

which shows that in the interaction picture the time evolution of the operators are found from the known part of the Hamiltonian, H_0 . Consider the example Hamiltonian, where c_k is the annihilation operator in the interaction picture,

$$\begin{aligned} H_0 &= \sum_k \hbar\omega_k c_k^\dagger c_k \\ [c_{k'}, H_0] &= \sum_k \hbar\omega_k [c_{k'}, c_k^\dagger] c_k \\ &= \hbar\omega_{k'} c_{k'} \\ \Rightarrow c_k(t) &= e^{-i\omega_k t} c_k \end{aligned} \quad (5)$$

Defining the time evolution operator in the interaction picture and deriving its form in terms of the different parts of the Hamiltonians;

$$\begin{aligned} |\Psi_I(t)\rangle &= U(t, t_0) |\Psi_I(t_0)\rangle \\ |\Psi_I(t)\rangle &= e^{iH_0t/\hbar} |\Psi_S(t)\rangle = e^{iH_0t/\hbar} e^{-iH(t-t_0)/\hbar} |\Psi_S(t_0)\rangle \\ &= e^{iH_0t/\hbar} e^{iH(t-t_0)/\hbar} e^{-iH_0t_0/\hbar} |\Psi_I(t_0)\rangle \end{aligned} \quad (6)$$

and

$$O_H(t) = U(0, t) O_I(t) U(t, 0) \quad (7)$$

We have also

$$i\hbar \frac{\partial}{\partial t} |\Psi_I(t)\rangle = H_I^{int}(t) |\Psi_I(t)\rangle \quad (8)$$

which combined with eq. (6) leads to

$$i\hbar \frac{\partial}{\partial t} U(t, t_0) = H_I^{int}(t) U(t, t_0).$$

Integrating, one finds

$$i\hbar U(t, t_0) - i\hbar U(t_0, t_0) = \int_{t_0}^t dt' H_I^{int}(t') U(t', t_0)$$

$$U(t, t_0) = 1 - \frac{i}{\hbar} \int_{t_0}^t dt' H_I^{int}(t') U(t', t_0) \quad (9)$$

$$U(t', t_0) = 1 - \frac{i}{\hbar} \int_{t_0}^{t'} dt'' H_I^{int}(t'') U(t'', t_0) \quad (10)$$

This shows how the time evolution operator U always can be replaced by an integral containing a new time variable, as eq. (10) can be put into eq. (9). This can be repeated infinitely, and then U can be written as a series [11][12]:

$$U(t, t_0) = 1 + \frac{-i}{\hbar} \int_{t_0}^t H_I^{int}(t') dt' + \frac{(-i)^2}{\hbar^2} \int_{t_0}^t dt' \int_{t_0}^{t'} dt'' H_I^{int}(t') H_I^{int}(t'') + \dots \quad (11)$$

Consider the third term. By noting that this is symmetric around the line $t' = t''$ one can instead of integrating over the triangle as done above, rather integrate over the full square ($t_0 < t' < t, t_0 < t'' < t$) and then divide by two [11][12]. Doing so, it is possible to write eq. (11) in a very compact way:

$$U(t, t_0) = T \left\{ \exp \left[-\frac{i}{\hbar} \int_{t_0}^t dt' H_I^{int}(t') \right] \right\} \quad (12)$$

Here we have again the fermionic time-ordering operator T which makes sure that the integrals in eq. 11 are reproduced by this new expression. T can be used here as well as now U is a function of fermionic field operators, as the interaction part of the Hamiltonian is expressed in second quantization.

2.1.2 History and future

Now we look more closely at the state vectors in order to express the exact ground-state Ψ_0 , in Heisenberg picture, in terms of the noninteracting ground state, which we simply will call $|0\rangle$. We see from eq. (8) that the evolution of the state vector $|\Psi_I(t)\rangle$ is governed by H^{int} , and $|0\rangle$ is non interacting, and thus cannot be affected by it. To solve this problem, consider a non-interacting state in the far history when H^{int} is switched off. Then, moving in time towards the present, the interacting part is turned on, and when the present is reached, we have the exact, interacting ground state. Formally this will be equivalent to

$$|\Psi_{0(H)}\rangle = |\Psi_I(0)\rangle = U(0, -\infty)|0\rangle \quad (13)$$

and it is a consequence of the Gell-Man and Low theorem, and a proof of this theorem can be found in [11]. Consider again eq. (2) in a situation when $t > t'$, and by making use of eq. (13) and (7) we find

$$\begin{aligned} G(\mathbf{x}, t, \mathbf{x}', t') &= \\ &= \frac{\langle 0|U(\infty, 0)U(0, t)\psi_I(\mathbf{x}, t)U(t, 0)U(0, t')\psi_I(\mathbf{x}, t)U(t', 0)U(0, -\infty)|0\rangle}{\langle 0|U(\infty, -\infty)|0\rangle} \\ &= \frac{\langle 0|U(\infty, t)\psi_I(\mathbf{x}, t)U(t, t')\psi_I(\mathbf{x}, t)U(t', -\infty)|0\rangle}{\langle 0|U(\infty, -\infty)|0\rangle}, \end{aligned}$$

which is a time ordered product, and it would have been even if $t < t'$, and this allows us to finally state

$$G(\mathbf{x}, t, \mathbf{x}', t') = \frac{\langle 0|T\{\psi_I(\mathbf{x}, t)\psi_I(\mathbf{x}', t')U(\infty, -\infty)\}|0\rangle}{\langle 0|U(\infty, -\infty)|0\rangle}. \quad (14)$$

where we now have succeeded in relating the Green's function to the noninteraction groundstate $|0\rangle$ and interaction picture field operators. The next challenge is to treat the time-ordering operator T .

2.1.3 Wick's theorem

According to Wick's theorem, also proved in [11], one can expand time ordered products as (suppressing \mathbf{x} for simplicity)

$$T\{\psi_I(t_1)\psi_I(t_2)\dots\} = N\{\psi_I(t_1)\psi_I(t_2)\dots\} + \text{"all possible contractions"}$$

where a contraction is defined as

$$\overline{\psi_I(t_1)\psi_I(t_2)} \equiv \begin{cases} [\psi_I^+(t_1), \psi_I^-(t_2)] & \text{if } t_1 > t_2 \\ [\psi_I^+(t_2), \psi_I^-(t_1)] & \text{if } t_1 < t_2 \end{cases}$$

where now the field operators are split into two parts; the one marked with "+" contains only annihilation operators and the one with "-" creation operators. Splitting the operators in this way also makes it easier to do the normal ordering in Wick's theorem. The normal ordering operator N moves all annihilation operators to the right, this is just what normally is called normal ordering, and due to the fermionic commutation relations, the sign changes every time two field operators changes place.

The expression "all possible contractions" means that all operators shall be contracted, in pairs, in all combinations. Every combination gives a term, and not all operators have to be contracted.

2.1.4 Example Hamiltonian

Formulating quantum mechanics in the way often referred to as the second quantization, the interaction part of the Hamiltonian is also formulated in field operators. Thus eq. (14) is an expression of time ordered field operators that we now can express in terms of contractions and normal ordered product thanks to Wick's theorem. From here one can proceed to expand any system in this perturbative manner, and for a thorough discussion the reader may consult [10][11][12]. For the relevance of this work, we will stay closer to our subject and study an example of phonon-electron interaction, and will follow the discussion in [13]. The interacting part of the Hamiltonian can be expressed as

$$H^{int} = \sum_q M_q a_{k+q}^\dagger a_k (b_q + b_{-q}^\dagger)$$

where a_k, a_k^\dagger are fermionic ladder operators and b_q, b_q^\dagger are their counterparts for phonons. Working in k -space, one can take the field operators simply to be $\psi_I(k, t) = a_k(t), \psi_I^\dagger(k, t) = a_k^\dagger(t)$, where we also assume the same time dependence as shown in eq. (5). In order to shorten the expressions, let $a_{k_2}(t_2) \equiv a_{k_2}$. Now, writing out eq. (14) in this system using eq. (12) to expand the time evolution operator, and suppressing the denominator yields

$$G(k_1, t_1, k_2, t_2) = \langle 0 | T \left\{ a_{k_1} a_{k_2}^\dagger \times \left[1 - \frac{i}{\hbar} \int dt' H_I^{int}(t') - \frac{1}{\hbar^2} \int dt' \int dt'' H_I^{int}(t') H_I^{int}(t'') \right] \right\} | 0 \rangle. \quad (15)$$

Wick's theorem states that the field operators should be normal ordered and contracted, but as the expression is squeezed between a non interacting vacuum, normal ordered operators will be destroyed, which is also the case for not fully contracted products. Keeping in mind that we now look for interactions in the system, we see that the 1 inside the bracket cannot support interactions. A closer investigation also shows that no contractions can make the second term interact, however, the third term will do just this, and we write out one possible set of contractions of that term:

$$\langle 0 | \int dt' \int dt'' a_{k_1}^\dagger a_{k_2}^\dagger \cdot \frac{1}{\hbar^2} \sum_{q, q'} M_q a_{k''+q}^\dagger a_{k''} (b_q + b_{-q}^\dagger) M_{q'} a_{k'+q'}^\dagger a_{k'} (b_{q'} + b_{-q'}^\dagger) | 0 \rangle.$$

Here the contractions tell the story of this particular matrix element. An electron excited at t_2 propagates to t'' , where a phonon is excited (take $q < 0$), both the phonon and electron propagates to a new time t' where the phonon is destroyed leaving its momentum to the electron which is then again annihilated at t_2 (the same thing is possible with the other phonon operators, but then with $q > 0$ and then direction of the momentum transfer reversed). The result of all different contraction that survive can be pictured in diagrams, as seen in fig. 5.

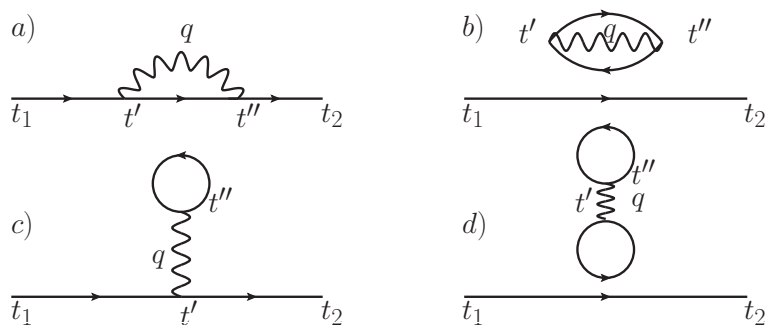


Figure 5: The first order of interacting diagrams for the H_{el-ph} .

Diagram a) is the one described by the contractions above (but with time reversed). From the diagram it is clear that t' and t'' can change place, and the momentum transfer can occur with some variety. It can be shown [10][11], that the disconnected parts of the diagrams (c and d) exactly cancel the denominator in eq (14), so we need to consider diagrams of type a) and b) only. Focusing again on diagram a), one can imagine higher order variations of this type. Including higher orders in eq.

(12) would create interactions after one another and mixed interactions as shown in fig. 6.

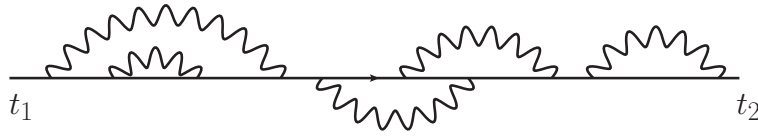


Figure 6: An example of a higher order diagram of type a) from fig. 5.

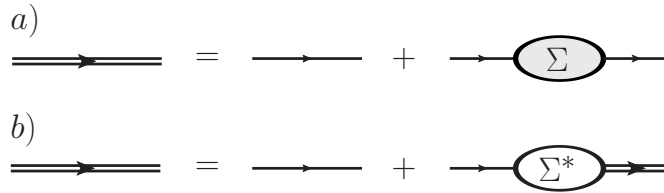


Figure 7: The self energy equations shown graphically, a) containing the total self energy Σ and b) the *proper self energy* Σ^* . The thin fermion lines are noninteracting Green's function whereas the double lines represent the fully interacting Green's function.

In fig. 7 we introduce a common way of describing diagrams without having to show the complicated structure of diagrams as in fig. 6. The simple line is now the zero order Green's function, G_0 , originating from the term 1 in eq. (15) with no interactions. Now, let Σ contain all interactions and loops that can fit between two such propagators. This is the Dyson equation, and the mathematical structure for a) in fig. 7 is

$$G(\mathbf{x}_1, t_1, \mathbf{x}_2, t_2) = G_0(\mathbf{x}_1, t_1, \mathbf{x}_2, t_2) + \iint dt' d^3x'' \iint dt'' d^3x''' G_0(\mathbf{x}_1, t_1, \mathbf{x}', t') \Sigma(\mathbf{x}', t', \mathbf{x}'', t'') G_0(\mathbf{x}'', t'', \mathbf{x}_2, t_2). \quad (16)$$

In fig. 7 b) another approach is taken as well, introducing the *proper self energy* to contain the simplest possible selfenergy expression capable of reproducing all orders in an iterative way as demonstrated in fig. 8. By ending that equation with the fully interacting Green's function, the solutions are found as a infinite series. The mathematical form for b) can similarly to eq. (16) be found as

$$G(\mathbf{x}_1, t_1, \mathbf{x}_2, t_2) = G_0(\mathbf{x}_1, t_1, \mathbf{x}_2, t_2) + \iint dt' d^3x' \iint dt'' d^3x''' G_0(\mathbf{x}_1, t_1, \mathbf{x}', t') \Sigma^*(\mathbf{x}', t', \mathbf{x}'', t'') G(\mathbf{x}'', t'', \mathbf{x}_2, t_2). \quad (17)$$

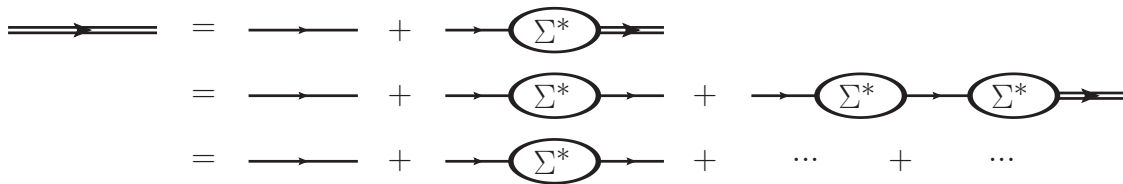


Figure 8: By iterating the Dyson equation b) from fig. 7 one regains all orders of the total self energy.

2.1.5 Self consistent Born approximation

In this work the number of different interactions are limited by the self consistent Born approximation. It is best presented graphically, as done in fig. 9.

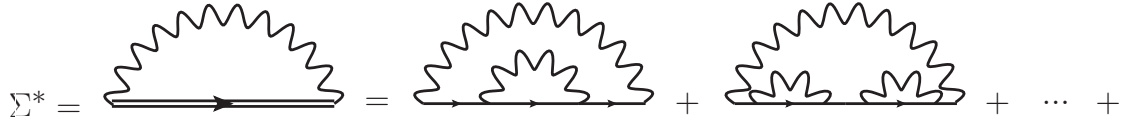


Figure 9: The proper self energy for the self consistent born approximation, where two possible terms are shown.

By including a noninteracting phonon line but the fully interacting Green's function one regains diagrams as the first part in fig. 6, although not the middle part, but then again the last part. This is the approximation made.

2.1.6 Eq. of motion for the Green's function

We will here derive the equations of motion for the non interacting Green's function G_0 , with respect to the diagonalizable part of the Hamiltonian

$$H_0 = -\frac{\hbar^2}{2m} \int d^3x \psi_H^\dagger(\mathbf{x}, t) \nabla^2 \psi_H(\mathbf{x}, t) + \int d^3x \psi_H^\dagger(\mathbf{x}, t) U(\mathbf{x}, t) \psi_H(\mathbf{x}, t).$$

Eq. (2) is now differentiated with respect to t_1 and by remembering that $\frac{\partial}{\partial t_1} \theta(t_1 - t_2) = \delta(t_1 - t_2)$, one finds

$$\begin{aligned} i\hbar \frac{\partial G_0(\mathbf{x}_1, t_1, \mathbf{x}_2, t_2)}{\partial t_1} &= \delta(t_1 - t_2) \frac{\langle \Psi_0 | \{ \psi_H(\mathbf{x}_1, t_1), \psi_H^\dagger(\mathbf{x}_2, t_2) \} | \Psi_0 \rangle}{\langle \Psi_0 | \Psi_0 \rangle} \\ &\quad - \frac{i \langle \Psi_0 | T \{ i\hbar \frac{\partial \psi_H(\mathbf{x}_1, t_1)}{\partial t_1} \psi_H^\dagger(\mathbf{x}_2, t_2) \} | \Psi_0 \rangle}{\langle \Psi_0 | \Psi_0 \rangle} \end{aligned} \quad (18)$$

where in the first term we now have a commutator times a delta function in time. As this term is zero unless $t_1 = t_2$ the anti-commutator will approach the usual equal time anti-commutator, which will result in the spatial delta function,

$$\{ \psi(\mathbf{x}_1), \psi^\dagger(\mathbf{x}_2) \} = \delta^3(\mathbf{x}_1 - \mathbf{x}_2)$$

while the second term will be governed by the time derivative of the field operator

$$\frac{\partial \psi_H(\mathbf{x}, t)}{\partial t} = [\psi_H(\mathbf{x}, t), H_0],$$

which with H_0 quickly gives

$$[\psi_H(\mathbf{x}, t), H_0] = -\frac{\hbar^2}{2m} \nabla^2 \psi_H(\mathbf{x}, t) + U(\mathbf{x}, t) \psi_H(\mathbf{x}, t).$$

In the Heisenberg picture we can move ∇ outside and write eq. (18) as

$$\left\{ i\hbar \frac{\partial}{\partial t_1} + \frac{\hbar^2}{2m} \nabla^2 - U(\mathbf{x}_1, t_1) \right\} G_0(\mathbf{x}_1, t_1, \mathbf{x}_2, t_2) = \delta(t_1 - t_2) \delta(\mathbf{x}_1 - \mathbf{x}_2)$$

which can be used with the Dyson equation (17) to establish

$$\begin{aligned} & \left\{ i\hbar \frac{\partial}{\partial t_1} + \frac{\hbar^2}{2m} \nabla^2 - U(\mathbf{x}_1, t_1) \right\} G(\mathbf{x}_1, t_1, \mathbf{x}_2, t_2) \\ &= \delta(t_1 - t_2) \delta(\mathbf{x}_1 - \mathbf{x}_2) + \int dt'' \Sigma(\mathbf{x}_1, t_1, \mathbf{x}'', t'') G(\mathbf{x}'', t'', \mathbf{x}_2, t_2). \end{aligned} \quad (19)$$

where the second integral from eq. (17) has been reduced with the help of the delta functions appearing. A similar expression can of course be obtained by differentiating t_2 .

2.2 Non-Equilibrium Green's functions

In this section we will show how to go from an equilibrium situation to a non-equilibrium one but still find good use of the Green's function formalism. Instead of looking into the far future, we let time be slightly complex in order for it to return and bite its own tail; touching this way only the far history. To make sense of it all we will introduce a road map to project the imaginary findings onto a physical world.

2.2.1 Contour ordering

As seen above, the Gell-Mann-Low theorem [11] allowed us to use the time evolution operators to switch on the interactions when approaching the present, and then again let the interaction die out when going to the far future. This symbolizes an equilibrium situation; the system is in a steady state, something happens, it reacts and then eventually goes back into its historic state. This is not true in a nonequilibrium steady state, where we start at equilibrium, and then after turning on the interactions we are left with a nonequilibrium steady state. The solution is to refine the idea of time-ordering the Green's function and instead order it along a complex contour in imaginary time, as shown in fig. 10.

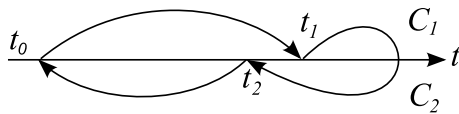


Figure 10: Upper, C_1 , and lower, C_2 , contour and two times, $t_{1/2}$, on the different contours. Note that they can be placed in arbitrary order.

By contour-ordering the Green's function instead of time-ordering it (eq. (20)), it can be shown, as done by Rammer and Smith [14], that the nonequilibrium theory is structurally equivalent to the equilibrium one, and this allows us again to expand perturbatively in diagrams and Dyson equations.

$$G(\mathbf{x}_1, t_1, \mathbf{x}_2, t_2) = \langle \Psi_0 | T_C \left\{ \psi_H(\mathbf{x}_1, t_1) \psi_H^\dagger(\mathbf{x}_2, t_2) \right\} | \Psi_0 \rangle \quad (20)$$

Different ordering As can be seen in fig. 10, t_1 and t_2 can be connected in many ways, and to distinguish the different Green's functions connecting the times, one often defines them in the following way:

contour-ordered	(G_c)	\equiv	$t_1, t_2 \in C_1$
anti-contour-ordered	$(G_{\bar{c}})$	\equiv	$t_1, t_2 \in C_2$
lesser	$(G^<)$	\equiv	$t_1 \in C_1, t_2 \in C_2$
greater	$(G^>)$	\equiv	$t_2 \in C_1, t_1 \in C_2$

Table 1: Contour ordering definitions

in addition, one often defines a *retarded* (that only lives prior to a time t) and a *advanced* (that only lives later than a point t) Green's function according to

$$G^r(\mathbf{x}_1, t_1, \mathbf{x}_2, t_2) = -i\theta(t_1 - t_2)\langle\Psi_0|\{\psi_H(\mathbf{x}_1, t_1), \psi_H^\dagger(\mathbf{x}_2, t_2)\}|\Psi_0\rangle \quad (21)$$

$$G^a(\mathbf{x}_1, t_1, \mathbf{x}_2, t_2) = i\theta(t_2 - t_1)\langle\Psi_0|\{\psi_H(\mathbf{x}_1, t_1), \psi_H^\dagger(\mathbf{x}_2, t_2)\}|\Psi_0\rangle \quad (22)$$

2.2.2 Langreth theorem

In order to relate the imaginary parts of our new nonequilibrium formalism to the real time, we will here present some result by Langreth [15]. They show how to use analytic continuation to transform quantities of the type

$$C(t_1, t_2) = \int_C d\tau A(t_1, \tau)B(\tau, t_2) \quad (23)$$

with complex time τ to the real axis. Langreth also shows how to deal with parallel lines in the diagrammatic perturbation expansion, such as in fig. 5 a, which has the structure of (and also with the τ dependence interchanged).

$$C(\tau_1, \tau_2) = A(\tau_1, \tau_2)B(\tau_2, \tau_1) \quad (24)$$

The results crucial to our discussion will be presented here in a compact form, where $C = \int_C AB$ implies eq. (23).

	Contour	Real axis
1.	$C = \int_C AB$	$C^< = \int_t [A^r B^< + A^< B^a]$ $C^r = \int_t A^r B^r$
2.	$D = \int_C ABC$	$D^< = \int_t [A^r B^r C^< + A^r B^< C^a + A^< B^a C^a]$ $D^r = \int_t A^r B^r C^r$

Table 2: A summary of the most important rules for going from the contour to the real axis. Table to large extent taken from [13].

2.2.3 The equations of motion in real time

In the sixties two proposals were made on how to establish the equations of motions for the nonequilibrium Green's functions, known as the Kadanoff-Baym and Keldysh

methods [16][17]. The aim of both methods is to find an expression for $G^{>/<}$ and we will here simply give the main result by Keldysh, taken from [13], with suppressed variables (time, space)

$$G^< = \int_{t'} \int_{t''} [(1 + G^r \Sigma^r) G_0^< (1 + \Sigma^a G^a) + G^r \Sigma^< G^a] \quad (25)$$

The first term is due to initial correlations, and gives the information about the starting conditions for the system. In this work, we are not interested in this but rather the steady state when all small initial condition have died out long ago. We therefore disregard that term, keeping only the last one.

Using the rules in table 2 we can formulate the equations of motions (19) for retarded and lesser Green's functions in real time;

$$\begin{aligned} & \left\{ i\hbar \frac{\partial}{\partial t_1} + \frac{\hbar^2}{2m} \nabla^2 - U(\mathbf{x}_1, t_1) \right\} G^<(\mathbf{x}_1, t_1, \mathbf{x}_2, t_2) \\ &= \int dt'' [\Sigma^r(\mathbf{x}_1, t_1, \mathbf{x}'', t'') G^<(\mathbf{x}'', t'', \mathbf{x}_2, t_2) + \Sigma^<(\mathbf{x}_1, t_1, \mathbf{x}'', t'') G^r(\mathbf{x}'', t'', \mathbf{x}_2, t_2)]. \end{aligned} \quad (26)$$

$$\begin{aligned} & \left\{ i\hbar \frac{\partial}{\partial t_1} + \frac{\hbar^2}{2m} \nabla^2 - U(\mathbf{x}_1, t_1) \right\} G^{\text{ret/adv}}(\mathbf{x}_1, t_1, \mathbf{x}_2, t_2) \\ &= \delta(t_1 - t_2) \delta(\mathbf{x}_1 - \mathbf{x}_2) + \int dt'' \Sigma^{\text{ret/adv}}(\mathbf{x}_1, t_1, \mathbf{x}'', t'') G^{\text{ret/adv}}(\mathbf{x}'', t'', \mathbf{x}_2, t_2). \end{aligned} \quad (27)$$

where the delta function vanishes for the lesser function, as the times are defined to be on the opposite sides of the contour. Equivalent expressions can be found for t_2 , and the the greater function as well, repeating the same steps.

2.3 Translational invariance and the Fourier transforms

In this section we leave the textbook discussion and the review of the Green's function formalism and instead venture into concepts central in this work. We follow mainly a manual for the program package used for the simulations in this work [18], a program developed by A. Wacker, S.-C. Lee and R. Nelander.

As we are to study QCLs which are periodic structures there is a translational invariance of the system, as the Green's function depends only on the difference in \mathbf{x}_1 and \mathbf{x}_2 , and the period and level index. At the same time there is an energy (or potential) difference, as the system is under a constant bias.

The basis states of the heterostructure will be quantized in the z -direction and treated as free in the x - and y -direction, consisting of plane waves with vectors \mathbf{k} :

$$\Phi_{\mathbf{k},\alpha}(z) = e^{i\mathbf{k}\cdot(x,y,0)} \varphi_\alpha(z) / \sqrt{A}, \quad (28)$$

where the normalization of the state is ensured by dividing by the area of the layers, and where α holds information about the level and period. Thus the creation and annihilation operators work by putting or removing particles of a certain \mathbf{k} in or from these basis states. This gives a matrix structure to the equations of motion, in the basis of the states in eq. (28). Limiting $U_{\alpha\beta}(\mathbf{x}, t) \rightarrow U_{\alpha\beta}(t)$ to be a time dependent

function only (but still dependent on period index), one can then perform the Fourier transforms of eqs. (26)(27)

$$\begin{aligned} & \left\{ i\hbar \frac{\partial}{\partial t_1} - \frac{\hbar^2}{2m} k^2 - \mathbf{U}(t_1) \right\} \mathbf{G}^<(\mathbf{k}, t_1, t_2) \\ &= \int dt'' [\boldsymbol{\Sigma}^r(\mathbf{k}, t_1, t'') \mathbf{G}^<(\mathbf{k}, t'', t_2) + \boldsymbol{\Sigma}^<(\mathbf{k}, t_1, t'') \mathbf{G}^r(\mathbf{k}, t'', t_2)]. \end{aligned} \quad (29)$$

$$\begin{aligned} & \left\{ i\hbar \frac{\partial}{\partial t_1} + \frac{\hbar^2}{2m} k^2 - \mathbf{U}(t_1) \right\} \mathbf{G}^{\text{ret/adv}}(\mathbf{k}, t_1, t_2) \\ &= \delta(t_1 - t_2) \mathbf{1} + \int dt'' \boldsymbol{\Sigma}^{\text{ret/adv}}(\mathbf{k}, t_1, t'') \mathbf{G}^{\text{ret/adv}}(\mathbf{k}, t'', t_2). \end{aligned} \quad (30)$$

where we in both equations find that the last integral transforms as a convolution, and that the delta function transforms to the identity matrix. From here on, bold capital letters will imply a matrix, and their sizes will be $(N + \sum \nu) \times (N + \sum \nu)$, where N is the number of periods and ν is the level index. A system of three periods with five states each gives 15×15 matrices.

Our Green's functions are still dependent on two times. In order to solve this we say that the steady state solution that we seek will be almost independent in time, but it oscillates due to the periodic external field. Then the solution is also periodic and depends only on the difference in time $t_1 - t_2$. We expand the periodic function $\mathbf{U}(t)$ in a Fourier series as

$$\mathbf{U}(t) = \sum_h \mathbf{U}_h e^{-ih\Omega t}. \quad (31)$$

We use this expression to truncate the Fourier series, including only the lowest but most prominent parts. This formulation makes it easy to get the Fourier transform even though we actually have an explicit time dependence, and this approach is discussed for example in [19].

With $\mathbf{U}(t)$ as a truncated Fourier series, it is possible to do another Fourier transform from time to frequency space. It is done by using the time difference $t = t_1 - t_2$ and it will actually consist of two transformations. One continuous; mapping $G(\mathbf{k}, t_1, t - t_1)$ to $G(\mathbf{k}, E)$, and one discrete, transforming the system according to the frequency of $\mathbf{U}(t)$, which now is assumed to have a simple periodic behavior. This is described in [20], and it will be defined in our case as

$$F_h(\mathbf{k}, E) = \frac{1}{\hbar} \int dt \frac{1}{T} \int_0^T dt_1 e^{ih\Omega t_1} e^{iEt/\hbar} F(\mathbf{k}, t_1, t_1 - t) \quad (32)$$

$$F(\mathbf{k}, t_1, t_2) = \frac{1}{2\pi} \int dE \sum_h e^{-E(t_1 - t_2)/\hbar} F_h(\mathbf{k}, E) e^{ih\Omega t_1} \quad (33)$$

and from this we can transform the equations of motion (29)(30) to energy space to get

$$\begin{aligned} & (E + h\hbar\Omega - E_k) \mathbf{G}_h^{\text{ret/adv}}(\mathbf{k}, E) \\ & - \sum_l \left(\mathbf{U}_{h-l} + \boldsymbol{\Sigma}_{h-l}^{\text{ret/adv}}(\mathbf{k}, E + l\hbar\Omega) \right) \mathbf{G}_l^{\text{ret/adv}}(\mathbf{k}, E) = \mathbf{1} \delta^{h0} \end{aligned} \quad (34)$$

$$\begin{aligned}
(E + h\hbar\Omega - E_k)\mathbf{G}_h^<(\mathbf{k}, E) - \sum_l (\mathbf{U}_{h-l} + \Sigma_{h-l}^{\text{ret}}(\mathbf{k}, E + l\hbar\Omega)) \mathbf{G}_l^<(\mathbf{k}, E) \\
= \sum_l \Sigma_{h-l}^<(\mathbf{k}, E + l\hbar\Omega) \mathbf{G}_l^{\text{adv}}(\mathbf{k}, E).
\end{aligned} \tag{35}$$

These now take the form of matrix equations of size $h \times h$, and they are only functions of E and \mathbf{k} . In the program, these are the equations that are implemented and solved self consistently together with the Keldysh relation.

The Fourier components of the Green's functions due to h According to eq. (34)(35) we can calculate the *Fourier components* of the Green's functions, and as seen in the equations, the Fourier components couple to each other. Depending on the value of h , the matrix equation shown in eq. (34) and (35) will increase in size quadratically. But at the same time as the calculations become more cumbersome, processes of higher intensity can be taken into account.

The $h = 0$ case keeps only one term from eq. (31) that is constant in time. This is just the constant potential over the structure due to the bias over the structure. The physics in the Green's functions produces in this limitation will describe the *stationary behavior* of the system.

The $h = 1$ case means that the external light field only interacts with one quanta with the electrons in the system. Now absorption and stimulated emission is possible, and by including this effect we can calculate the gain coefficient of the system.

Higher h . Increasing the h will give the system a possibility to exchange more quanta with the light field; for example, when $h = 2$ the higher harmonic field has double the frequency, and interactions of higher energies are possible. Allowing higher orders of this kind becomes more important when dealing with low frequencies from the start – when the frequency approaches 0, as does the energy and multiple photons are more likely.

2.3.1 Self energies Σ

Everything that is not diagonal in \mathbf{k} , i.e. breaks the translational invariance that is the fundamental aspect of H_0 , is treated in the self energies. This is where the scattering takes place, as it redistributes states in k -space.

A very important approximation is made in the evaluation of the self energies, as they are assumed only to depend on energy, and not on \mathbf{k} . The advantage of this approximation is that not as many calculations have to be carried out, (much less in fact). The self energies have been evaluated by the program developers and here we follow again [18]. A good discussion on scattering in a QCL can be found in [21].

Phonon scattering For phonon scattering a constant matrix element is used, as discussed in [20][22]. The self energy formulation should be interpreted as the mathematical formulation of fig. 9, with the interacting Green's function and one

single non-interacting phonon line. The phonons are treated as an Bose distribution at equilibrium. The self energies take the following form [22][20]:

$$\begin{aligned} \Sigma_{\alpha\alpha'}^<(E) &= \sum_{\beta\beta'} X_{\alpha\alpha'\beta\beta'}^{phon-} f_{Bose}(E_{phon}) \int_0^\infty dE_{k'} G_{\beta\beta'}^<(k', E - E_{phon}) \\ &+ \sum_{\beta\beta'} X_{\alpha\alpha'\beta\beta'}^{phon+} (f_{Bose}(E_{phon}) + 1) \int_0^\infty dE_{k'} G_{\beta\beta'}^<(k', E + E_{phon}) \end{aligned} \quad (36)$$

and for the retarded

$$\begin{aligned} \Sigma_{\alpha\alpha'}^{ret}(E) &= \sum_{\beta\beta'} X_{\alpha\alpha'\beta\beta'}^{phon-} (f_{Bose}(E_{phon}) + 1) \int_0^\infty dE_{k'} G_{\beta\beta'}^{ret}(k', E - E_{phon}) \\ &+ \sum_{\beta\beta'} X_{\alpha\alpha'\beta\beta'}^{phon+} f_{Bose}(E_{phon}) \int_0^\infty dE_{k'} G_{\beta\beta'}^{ret}(k', E + E_{phon}) \\ &+ \frac{1}{2} \sum_{\beta\beta'} X_{\alpha\alpha'\beta\beta'}^{phon-} \int_0^\infty dE_{k'} G_{\beta\beta'}^<(k', E - E_{phon}) \\ &- \frac{1}{2} \sum_{\beta\beta'} X_{\alpha\alpha'\beta\beta'}^{phon+} \int_0^\infty dE_{k'} G_{\beta\beta'}^<(k', E + E_{phon}) \end{aligned} \quad (37)$$

where we have $f_{Bose} = 1/(\exp(E_{phon}/k_B T) - 1)$ for the Bose distribution. Longitudinal optical phonons and acoustic phonons are treated in the same way but with different energies. The principal parts appearing in [22] and [20] is not shown as they are neglected in the calculations of this work.

Elastic scattering When evaluating the self energies for the impurity scattering, alloy scattering and interface roughness scattering we proceed by a general expression for the self energy structure in the self consistent Born approximation [23].

$$\Sigma_{\alpha\alpha'}^{</ret}(\mathbf{k}, E) = \sum_{\beta\beta'} \sum_{\mathbf{k}'} \langle V_{\alpha\beta}(\mathbf{k} - \mathbf{k}') V_{\beta'\alpha'}(\mathbf{k}' - \mathbf{k}) \rangle G_{\beta\beta'}^{</ret}(k', E) \quad (38)$$

$V_{\alpha\beta}$ is here the matrix elements for the scattering potential. The angle brackets indicate that the elastic scattering is included on an average basis over the surfaces or over the impurities in the system, for example. Following [22], the calculations are simplified by instead of evaluating the interactions of all possible values of \mathbf{k} some typical values are chosen. Then, the summation over \mathbf{k} is turned into an integral over the energies E_k instead, and the average matrix elements are now independent of E_k and they are taken out. The general form of the elastic self energies can then be written as

$$\Sigma_{\alpha\alpha'}^{</ret}(E) = \sum_{\beta\beta'} X_{\alpha\alpha'\beta\beta'}^{elast} \int_0^\infty dE_{k'} G_{\beta\beta'}^{</ret}(k', E) \quad (39)$$

in accordance with the self consistent Born approximation illustrated in fig. 9, and the matrix elements represent the average strength of the scattering. This average

and the use of typical energies in the calculations allows for a treatment where the matrix elements are constant in momentum $\mathbf{k} - \mathbf{k}'$. This means they do not have to be evaluated for each E_k point in the discrete grid.

The calculation of each matrix element is a cumbersome process and will not be repeated here. The interested reader should consult [22] for a discussion on the scattering rates of impurities and interface roughness potentials used in this work. An introductory approach to alloy scattering can be found in [21].

2.3.2 Mean field potential

In order to account for some of the Coulomb interactions a mean field is included in U . This is calculated from the Poisson equation and is included in the Hamiltonian as

$$U_{\alpha,\alpha',h}^{MF} = e \int dz \varphi_{\alpha}(z) \phi_h^{MF}(z) \varphi_{\alpha'}(z) \quad (40)$$

where the $\varphi(z)$ are the ones introduced in eq. (28), and ϕ^{MF} is the mean field as a function in z .

2.3.3 EM-field in Lorenz gauge

In Lorenz gauge which is used in the calculations, we use for $|h| \leq 1$

$$\mathbf{U}_{\pm 1} = -\frac{eF_{ac}d}{2}\mathbf{z} \quad (41)$$

where \mathbf{z} holds the information of the wavefunctions overlap according to

$$z_{\beta\alpha} = \frac{1}{d} \int dz z \varphi_{\beta}^*(z) \varphi_{\alpha}(z).$$

and F_{ac} is the strength of the oscillating electromagnetic field at the given frequency. This couples the states and make optical transitions possible.

2.4 A simple model of gain between subband states

In this section a simple model of the gain between subbands will be established that will be closely related to the oscillator strength. It is an expression valuable when we are to *interpret* the calculations by the more sophisticated model, and it also allows us to make an estimate of the integrated absorption in the system we are studying. The equation reads

$$G(\omega) = \frac{e^2 |z_{lo,up}|^2 \omega (n_{up} - n_{low})}{2dc\epsilon_0 \sqrt{\epsilon_r}} \frac{\Gamma}{(E_{up} - E_{lo} - \hbar\omega)^2 + \Gamma^2/4} \quad (42)$$

where $z_{lo,up}$ is the dipole matrix element, $n_{up/lo}$ is the densities of the upper and lower levels, d is the period of the structure, Γ is a broadening, i.e. the full width maxima, ω is the frequency and E is the energies for the different states.

The matrix elements entering the expression will be examined and described, and finally a expression for integrated absorption between subbands will be derived using the Tomas Reiche-Kuhn sum rule for oscillator strengths.

2.4.1 Modal gain

We will derive eq. (42), following [8], starting from Fermi's golden rule, neglecting spontaneous emission, and an electromagnetic field \mathbf{F} polarized in the z -direction and propagating, for simplicity, in the y -direction (although the x -direction is equivalent in the case of specified growth direction along z);

$$\begin{aligned} \mathbf{F}(\mathbf{r}, t) &\equiv F_0 \mathbf{e}_z \cos\left(\frac{\sqrt{\epsilon_r}\omega}{c}y - \omega t\right) \\ \Rightarrow \mathbf{A}(\mathbf{r}, t) &= \frac{F_0 c \mathbf{e}_z}{-i\omega} \cos\left(\frac{\sqrt{\epsilon_r}\omega}{c}y - \omega t\right) \end{aligned} \quad (43)$$

with ω as the frequency of the field, $k = \sqrt{\epsilon_r}\omega/c$ and F_0 the amplitude of the electric field. A general formulation of the Fermi's golden rule for stimulated emission is [24]

$$R_{up \rightarrow lo}(\mathbf{k}) = \frac{2\pi}{\hbar} |V_{up,lo}(\mathbf{k})|^2 \delta(E_{up} - E_{lo} - \hbar\omega)$$

where $V_{up,lo}$ is now the coupling between the states. This can be calculated from the electromagnetic part of the Hamiltonian, given by $-\mathbf{A} \cdot \hat{\mathbf{p}}/2m_e c$. This is justified if $\nabla \cdot \mathbf{A} = 0$ which holds for eq. (43). The vector potential can be expressed as

$$\begin{aligned} \mathbf{A}(\mathbf{r}, t) &= \frac{F_0 c \mathbf{e}_z}{-2i\omega} [e^{i\sqrt{\epsilon_r}\omega/c \cdot y - i\omega t} + e^{-i\sqrt{\epsilon_r}\omega/c \cdot y + i\omega t}] \\ &\rightarrow \frac{F_0 c \mathbf{e}_z}{-2i\omega} e^{-i\sqrt{\epsilon_r}\omega/c \cdot y + i\omega t} \end{aligned}$$

if we only keep the $e^{i\omega t}$ term that is responsible for stimulated emission. Continuing by calculating the coupling \mathbf{V} , the expression can be simplified further as we are working in a system where the wavelength of the light field is much larger than the system size. We can then apply the electron dipole approximation, setting

$$e^{-i\sqrt{\epsilon_r}\omega/c \cdot y} = 1.$$

$$\begin{aligned} V_{up,lo}(\mathbf{k}) &= -\frac{e}{4m_e c} \langle lo | \mathbf{A} \cdot \hat{\mathbf{p}} | up \rangle \\ &= \frac{eF_0 c}{4m_e c \omega} e^{i\omega t} e^{-i\omega t} \langle lo | \mathbf{e}_z \cdot \hat{\mathbf{p}} | up \rangle \\ &= \frac{eF_0}{m_e \omega} \langle lo | \hat{p}_z | up \rangle(\mathbf{k}) \end{aligned}$$

gives a modified Fermi's golden rule as

$$R_{up \rightarrow lo}(\mathbf{k}) = \frac{2\pi}{\hbar} \left| \frac{eF_0 \langle lo | \hat{p}_z | up \rangle(\mathbf{k})}{4m_e \omega} \right|^2 \delta(E_{up} - E_{lo} - \hbar\omega) \quad (44)$$

with

$$\begin{aligned} \langle lo | \hat{p}_z | up \rangle(\mathbf{k}) &= \frac{1}{A} \int d^3x \varphi_{up}^*(z) e^{-i(k_x x + k_y y)} \hat{p}_z \varphi_{lo}(z) e^{i(k_x x + k_y y)} \\ &= \frac{1}{A} \int dx dy \int dz \varphi_{up}^*(z) \hat{p}_z \varphi_{lo}(z) \\ &= \int dz \varphi_{up}^*(z) \hat{p}_z \varphi_{lo}(z) \\ &= \langle lo | \hat{p}_z | up \rangle \end{aligned}$$

where the factor $1/A$ comes from the normalization of the basis states. Now to calculate the gain in this system, let us consider a box of dimensions $L_x L_y L_z$. The enhancement of the field, i.e. the gain will be the energy contributed by stimulated emission, that is the number of photons emitted times the energy of them, so

$$P_{gain} = \frac{dN_{photons}}{dt} \hbar\omega$$

where we now can get the photons emitted from eq. 44 if we take into account the occupations. Summing over spins and over k of the occupation densities $f_{up/lo}(k)$ of the upper and lower level we get

$$\frac{dN_{photons}}{dt} = \frac{2\pi}{\hbar} \left| \frac{eF_0 \langle lo | \hat{p}_z | up \rangle(\mathbf{k})}{4m_e \omega} \right|^2 \delta(E_{up} - E_{lo} - \hbar\omega) \cdot 2 \sum_k [f_{up}(k) - f_{lo}(k)]$$

The gain will now be the relative increase in intensity over the propagation direction, and comparing incoming and outgoing intensities, we have, expressing the intensity as a function of y ,

$$g = \frac{I(L_y) - I(0)}{I(0)L_y} = \frac{P_{gain}}{I(0)AL_z}.$$

The average intensity we get from the Poynting vector as

$$I(y) = \frac{|F_0|^2}{2} \sqrt{\epsilon_r} \epsilon_0 c$$

and seeing that the sum over k of the occupation densities yields $A(n_{up} - n_{lo})$, we can put it all together, and we also replace the delta function with a Lorentzian broadening as

$$\delta(E_{up} - E_{lo} - \hbar\omega) = \frac{\Gamma}{2\pi(E_{up} - E_{lo} - \hbar\omega)^2 + \Gamma^2/4}. \quad (45)$$

We get a function for the gain as

$$G(\omega) = \frac{e^2 |\langle lo | \hat{p}_z | up \rangle|^2}{8d\sqrt{\epsilon_r \epsilon_0} cm_e^2 \omega} \frac{\Gamma}{(E_{up} - E_{lo} - \hbar\omega)^2 + \Gamma^2/4} \quad (46)$$

If the upper and lower states are now energy eigenstates, one can show that by $[\hat{z}, H_0] = \frac{i\hbar p_z}{m_e}$ we get

$$\begin{aligned} \langle lo | \hat{p}_z | up \rangle &= \frac{m_e}{i\hbar} \langle lo | [z, H_0] | up \rangle \\ &= \frac{m_e}{i\hbar} \langle lo | z | up \rangle (E_{up} - E_{lo}) - \langle lo | z | up \rangle (E_{lo} - E_{up}) \\ &= \frac{m_e}{i\hbar} 2(E_{up} - E_{lo}) \langle lo | z | up \rangle \end{aligned} \quad (47)$$

which allows for replacement of the matrix element, and brings us to eq. (42).

2.5 Integrated absorption

The simple model of gain summarized in eq. (43) can be used to calculate absorption as well, by changing the sign. Here we derive an expression for the *integrated absorption* of a heterostructure with the help of the Thomas Reiche Kuhn sum rule.

2.5.1 Thomas Reiche Kuhn sum rule [1][2]

Consider another expectation value with a arbitrary energy eigenstate i , and let H_0 full fill the property $[z, H_0] = \frac{i\hbar p_z}{m}$. This proof follows the one found in [24].

$$\begin{aligned} \langle i | [z, [z, H_0]] | i \rangle &= \langle i | z [z, H_0] - [z, H_0] z | i \rangle \\ &= \sum_n \langle i | z | n \rangle \langle n | [z, H_0] | i \rangle - \langle i | [z, H_0] | n \rangle \langle n | z | i \rangle \\ &= \sum_n \langle i | z | n \rangle \langle n | z | i \rangle (E_i - E_n) - \langle i | z | n \rangle \langle n | z | i \rangle (E_n - E_i) \\ &= \sum_n |\langle i | z | n \rangle|^2 \cdot 2(E_i - E_n) \end{aligned}$$

Combined with

$$\begin{aligned} \langle i | [z, [z, H_0]] | i \rangle &= \langle i | [z, \frac{i\hbar \hat{p}_z}{m_e}] | i \rangle \\ &= \frac{i\hbar}{m_e} \langle i | \frac{i\hbar}{m_e} | i \rangle \\ &= \frac{-\hbar^2}{m_e} \end{aligned}$$

we get

$$\sum_n \frac{2\omega_{ni}m_e}{\hbar} |\langle i|z|n\rangle|^2 = 1. \quad (48)$$

This shows how we can replace many parameters in eq. (42) if we sum over all states, and this is the main idea behind calculating the integrated absorption.

2.5.2 Subband absorption

Here we derive a formula for the integrated absorption of the subbands, which is the sum of all absorption at all possible frequencies between all subband states, similar to the derivation in [25].

$$\alpha(\omega) = \sum_{j,i} \alpha_{i \rightarrow j}(\omega) \theta(E_j - E_i)$$

where the Heaviside function ensures that only absorption is considered. Using eq. (43) for the two level absorption and integrating over the whole frequency spectra, using the delta function instead of the Lorentzian as described in eq. (45) we get

$$\alpha_{\text{int}} \equiv \int d\omega \alpha(\omega) = \sum_{j,i} \frac{\pi e^2 |z_{ji}|^2 (E_j - E_i) (n_i - n_j)}{\hbar^2 d c \epsilon_0 \sqrt{\epsilon_r}} \theta(E_j - E_i).$$

This double sum can be simplified by using the Thomas Reiche Kuhn sum rule presented above in eq. 48. If this is carried out with respect to j , and if it is assumed that the lower state i is much more populated than the upper state, one ends up with

$$\alpha_{\text{int}} = \sum_i \frac{\pi e^2 n_i}{2m_e^* d c \epsilon_0 \sqrt{\epsilon_r}}$$

as the Heaviside function is no longer required. Inserting $n_{av} = \sum_i n_i / d$ as the average three dimensional carrier distribution yields

$$\alpha_{\text{int}} = n_{av} \frac{\pi e^2}{2m_e^* c \epsilon_0 \sqrt{\epsilon_r}} \quad (49)$$

where we have an expression for the integrated absorption that is general and not dependent on neither structure nor bias, only doping density, effective mass and dielectric properties.

2.6 Basis States

The basis states for the calculation are chosen in order to simplify the calculation as much as possible, and in the case of a biased heterostructure with a periodic repetition the Wannier States are an optimal choice. These states will not change as the bias is changed, leaving matrix elements and other properties of the basis states unchanged. To get energy eigenstates, the Wannier states can be recalculated at a specific bias to Wannier-Stark states.

2.6.1 Wannier States

We give here a short summary of the derivation following [22]. The Schrödinger equation is solved with respect to the heterostructure only, in a transfer matrix approach. Using the Bloch condition $u_q(z + d) = e^{iqd}u_q(z)$, where d is still the period length, one can solve the transfer matrix equations giving the allowed energy eigenvalues as functions of q spanning the minibands in the structure. Then the Wannier functions are given as a superposition of Bloch functions as

$$\psi_\nu^W(z - nd) = \sqrt{\frac{d}{2\pi}} \int_{\pi/d}^{\pi/d} dq e^{-inqd} u_q^\nu(z) \quad (50)$$

where ν is the miniband index, and n selects neighboring periods. These Wannier functions can be constructed in many different ways, but they are chosen to be as localized as possible in order to reduce the mixing of states in each period. In this formalism, the annihilation and creation operators will be defined as

$$a_q^\nu = \sqrt{\frac{d}{2\pi}} \sum_n e^{-iqnd} a_n^\nu \quad a_q^{\nu\dagger} = \sqrt{\frac{d}{2\pi}} \sum_n e^{iqnd} a_n^{\nu\dagger}$$

where the index notation shows in which period and in which miniband the creation or annihilation is taking place.

2.6.2 Wannier-Stark states

If a bias is applied to the structure, the Wannier functions of a specific miniband will not all have the same energy, but will be separated by the potential difference between the period, in what is called a *Wannier-Stark ladder*. To get the energy eigenstates, one can diagonalize the new system with respect to the *Wannier-Stark* Hamiltonian

$$H_{WS} = H_W - eFz_{\alpha\beta} + U_{\alpha\beta}$$

where H_W is the Hamiltonian for the Wannier states and the potential is added with the coupling between states as well as the mean field $U_{\alpha\beta}$. The eigenfunctions one gets from diagonalizing this Hamiltonian will be energy eigenstates.

2.7 Gain calculated with the Green's functions

The gain in a material can be related to the conductivity;

$$\sigma(\omega) = \frac{\delta\langle J_0 \rangle(\omega)}{\delta F(\omega)}$$

where J_0 is the stationary current (rectified response) and F is the field strength at the given frequency. J_0 is calculated in from the Green's functions and then the gain is found by the relation

$$G(\omega) = -\frac{\Re\{\sigma(\omega)\}}{c\epsilon_0\sqrt{\epsilon_r}}$$

which with all the expressions inserted and weighted yields [23]

$$G_{up,lo}(\omega) = \frac{e^2 |z_{lo,up}|^2 \omega}{2dc\epsilon_0 \sqrt{\epsilon_r}} \frac{2}{A} \sum_{\mathbf{k}} \int \frac{dE}{2\pi} [\Im\{G_{up,up}^<(\mathbf{k}, E + \hbar\omega)\} A_{lo}(\mathbf{k}, E) - A_{up}(\mathbf{k}, E + \hbar) \Im\{G_{lo,lo}^<(\mathbf{k}, E)\}]. \quad (51)$$

Here $A(\mathbf{k}, E) = i[G^{ret}(\mathbf{k}, E) - G^{adv}(\mathbf{k}, E)]$ is the spectral function containing the density of states as a function of \mathbf{k} and E . Note that this is only valid for two levels, just as eq. (43). In the derivation following [23], only the stationary Green's functions are used in the expression above, i.e. the Green's function with $\hbar = 0$ in the matrix equations (35)(34) above. Also, the counter rotating terms have been neglected. Eq. (51) is similar to the modal gain in eq. (42) with the occupations and Lorentzian replaced by the expression containing the Green's functions and the spectral functions. The first term in this last expression can be interpreted as stimulated emission; electrons in *occupied* states in the upper level (the lesser Green's function) going to *empty* states (spectral function) in the lower level. The second term should then be interpreted as absorption; electrons in the lower level going to the upper level. The difference will constitute the resulting enhancement of the field.

This is only a simple and illustrative way of calculating the gain, and this is not the expression used in the program. There, instead a more complicated expression based on the *rectified response* J_1 is used to calculate gain.

3 Results

Below the results will be presented and discussed. The main part of this work have been simulations and thus the results have been collected by running the NEGFT program code, developed by A. Wacker with coworkers, in order to theoretically evaluate QCL properties. When making theoretical predictions and using a large computer program it is important to understand the underlying physics to be able to interpret the results, so discussions will follow the data presented.

A structure studied in an article by Burghoff *et al.* [6] is presented below, and a big part of this work aims at reproducing their experimental results. To do this we look first at linear response of the structure, then we regard nonlinear response. Also, convergence issues are addressed, computational problems with the k -space and e - e -scattering are discussed, and material parameters are investigated, before moving on to the conclusions.

3.1 Reference results

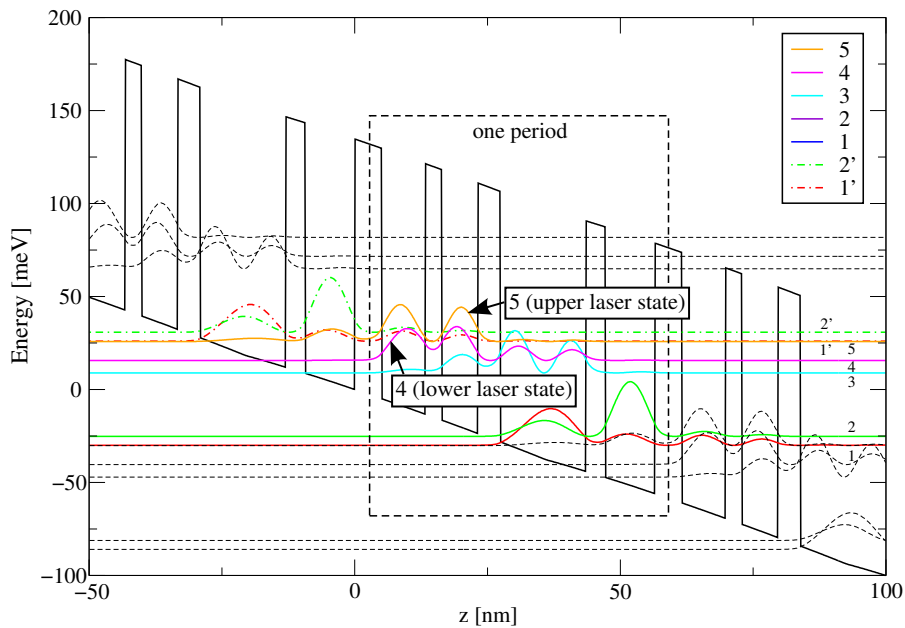


Figure 11: The QCL structure described in [6] at a bias of 56 mV/period. Five states from each period are shown in the plot, emphasizing the central period with two neighboring periods, and they are the calculated Wannier-Stark states that are energy eigenstates. The states are labeled in the figure, and the states indexed with a prime are from the leftmost period while the unprimed are from the central region. On the horizontal axis we have z which is the growth direction.

We will in the Results section study the linear and non linear response of a specific structure that has been studied to some extent in an article by Burghoff *et al.* [6]. It is a QCL based on five states in each active region; one injector state (1), one upper (5) and two lower laser states (3)(4), and one extraction state (2). At operating bias of 56 mV per period the states are aligned according to fig 11, and

from here on, state 5 (4) will often be called the upper (lower) laser state. The response of the structure, the gain and absorption, to an external field is measured in this article [6], and their main results are shown in fig. 12 and fig. 13. Fig 12a

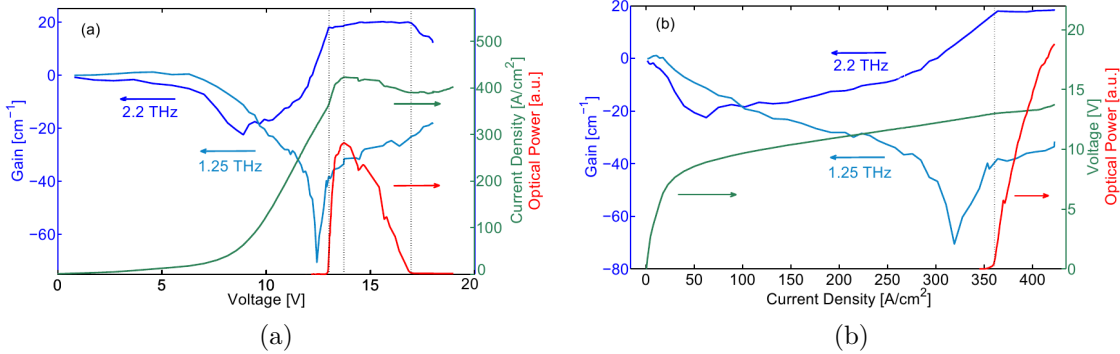


Figure 12: Plotted experimental data, figures taken from [6]. Optical power, absorption/gain at 2.2 THz and 1.25 THz and I-V characteristics plotted against bias (a) and current (b).

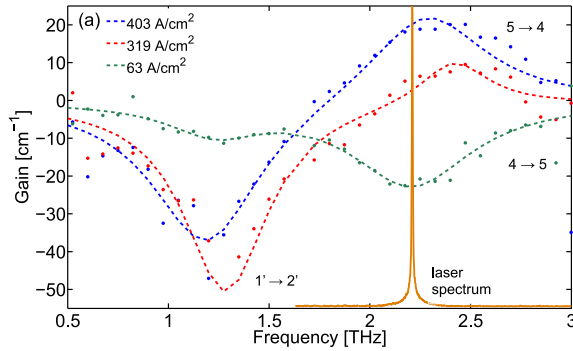


Figure 13: Plotted experimental data, figure taken from [6], of the measured gain at three different currents through the structure. The authors have also fitted double Lorentzian to their data points.

shows the current-to-voltage behavior (green), also known as the I-V characteristics, with the bias on the x -axis. Fig. 12b, on the contrary, has current on the x -axis. In addition, each plot shows optical power (red) as well as gain/absorption at the two frequencies 2.2 THz (dark blue) and 1.25 THz (turquoise). The lower plot (fig. 13) shows a very interesting set of measured data. Here the gain/absorption spectra is plotted for three different currents. There is also an inclusion of the laser spectrum, which is seen as a peak (orange) at 2.2 THz. These results are obtained by probing the structure at the different currents with an external light field, and looking at the changes of that field. This was done by coupling a pump laser of 125 mW with a spot size of about $20 \mu\text{m}$ onto a facet that measured $80 \times 10 \mu\text{m}^2$.

Although the structure has a broad gain spectrum capable of gain at more frequencies than 2.2 THz, as seen in fig. 13, the heterostructure is encapsulated in a metal-metal waveguide. This waveguide acts in a selective way, as the geometry of it allows only for specific wavelengths. As a consequence, the laser spectrum is almost

discrete. To summarize, Burghoff *et al.* [6] interprets the results by explaining what happens in the structure as bias increases; first at 63 A cm^{-2} current has started to flow through the structure due to an alignment of the groundstate and the lower laser state. This populates the lower laser state and absorption is then seen from the lower laser state to the higher laser state (green curve in fig. 13). Then at 319 A cm^{-2} the current is much higher, but the gain spectra reaches only 10 cm^{-1} (red curve in fig. 13). They also report that the internal losses of the cavity is 18 cm^{-1} , so the structure is not yet at operating bias. Finally at 403 A cm^{-2} the gain is at a level of 20 cm^{-1} at the lasing frequency and lasing is possible (blue curve in fig. 13). This measurement presents a perfect opportunity to see how well we can simulate the behavior in comparison to the experiment. Gain is often a hard thing to measure in experiments, and in this article both I-V characteristics and gain is now available.

3.2 Description and classification of the QCL

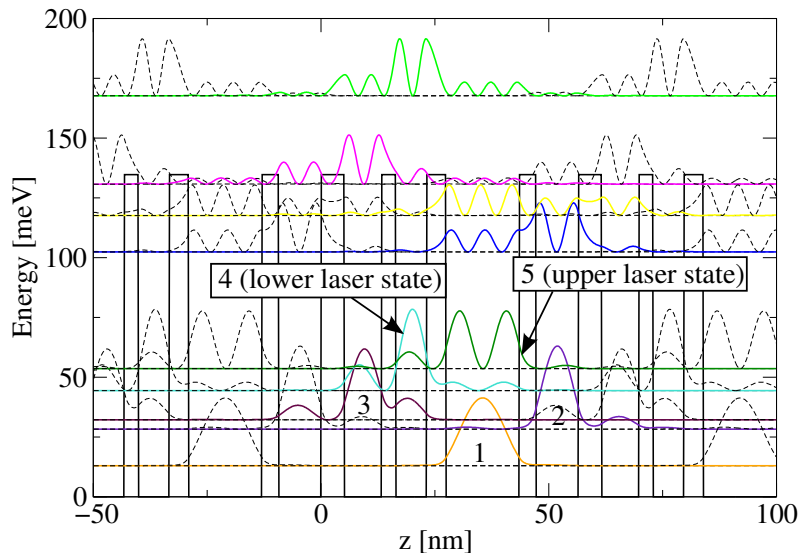


Figure 14: In this plot the nine first Wannier states are shown at zero bias to visualize the periodicity of the states and to show the unbiased heterostructure. The states of the central period are colored while the states of the neighboring periods are left dashed. Note that the ninth state is in the continuum.

The QCL studied here is a layered structure of $\text{Al}_{0.15}\text{Ga}_{0.85}\text{As}$ and GaAs . It is a QCL design based on a direct transition between the upper (5 in fig. 11) and lower lasing state (4 in fig. 11), and a quick resonant phonon depopulation of the lower lasing state, similar to the one presented in [26]. The decomposition is; **5.1**/**8.1**/**3.1**/**6.8**/**4.2**/**16.1**/**3.7**/**9.3** nm, with bold font for barriers. The thickest well is doped resulting in a sheet density of $3 \cdot 10^{10} \text{ cm}^{-2}$ carriers per period. At zero bias, the states are localized in an obvious periodic manner, shown in fig. 14. When bias is turned on, states will start to align, making tunneling through the barriers more probable, and current will flow through the structure. Another important aspect of the structure is the number of states in the structure. For low bias transport

only the lower five states in fig. 14 will be of importance, as we work at pretty low temperatures where the higher states always will be almost depopulated. At higher biases, and for a complete absorption spectra, the higher states will be of relevance. In the experiment performed in [6], 175 periods of the active region described above were included in the final structure, and the heterostructure was surrounded by a metal-metal waveguide. The sample was placed in a cryostat which was cooled to about 33 K.

3.3 Interface Roughness Scattering Parameter

The measurements on the structure presented in [6] offer an opportunity to calibrate a discussed parameter that is important in our simulation. The parameter is the average height of interface allocations, illustrated in figure 15. As the interfaces of the QCL are not perfect monolayers, there will be some islands of different material, giving a potential difference. Two parameters give the code the necessary information: the typical size of these islands λ , and the average height of the disturbing potentials η_j . Three different values of η have been tried: 0.14, 0.20 and 0.28. Depending on what parameter is used, the current and gain results changes.

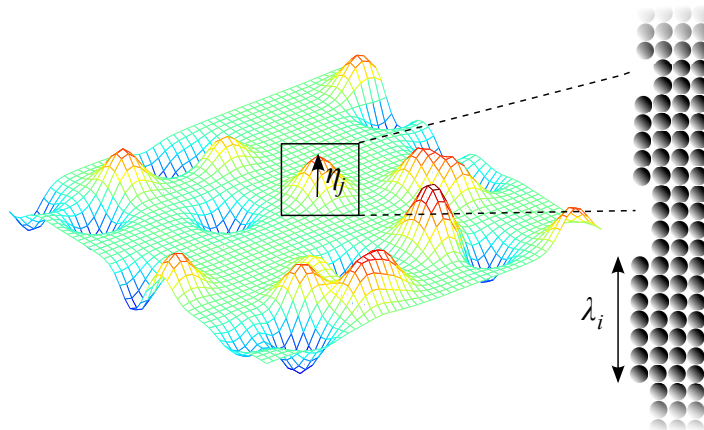


Figure 15: Imperfect monolayers gives rise to random potentials causing interface scattering. η is the root mean square of a statistical number of roughness impurity heights η_j and λ is the typical size among all λ_i .

Gain for biases at the peak operation point is shown in figure 17b and an increase in gain for the 10 meV transition at 58 mv/period by a factor of three is visible. Scattering decreases the lifetime of a state in the system, and for our laser we want high lifetime for the upper lasing state compared to the lower. In this case we benefit from less scattering, implying that state 5' is perhaps no longer easily scattered. The lower lasing state however can be deexcited by a optical phonon, which matches the energy gap, so the less roughness parameter is not as important in this case, as the fastest scattering factor will be of most importance in determining the lifetime. One can see from figure 16 that we have more current with higher scattering constants and that the double peak behavior is showing up again when we go to lower temperatures or lower values of η . At high bias, 50 mV/period as in figure 17a, we see

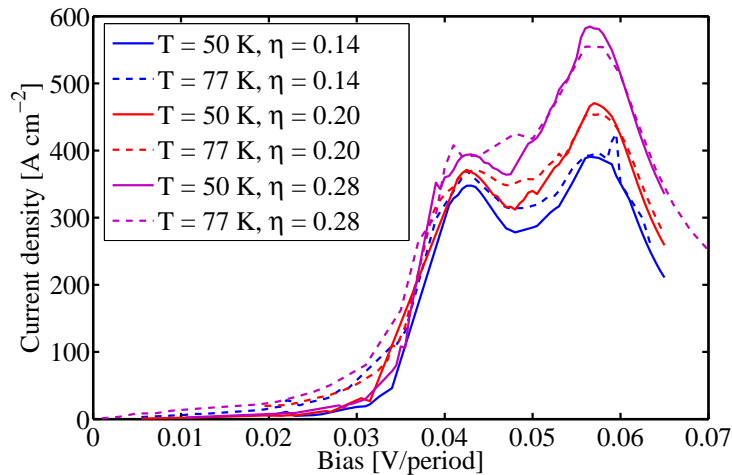


Figure 16: Current for three different samples with different interface roughness constants and different temperatures. Full lines correspond to 50 K whereas dashed lines correspond to 77 K.

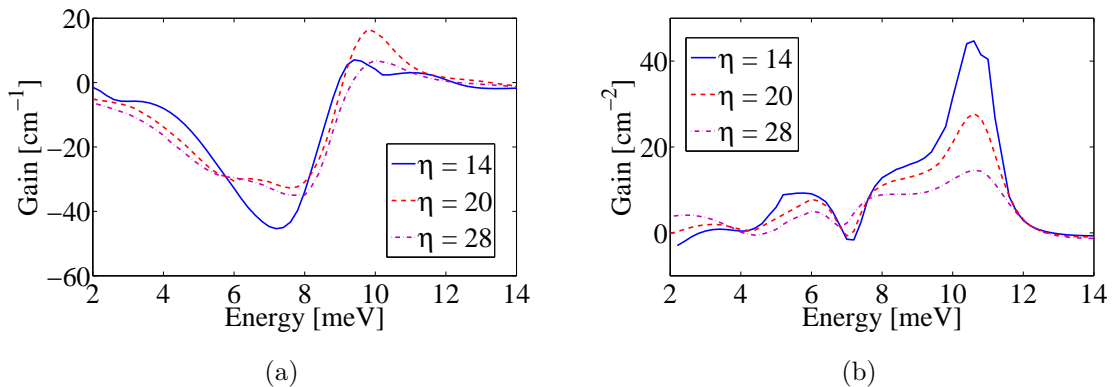


Figure 17: Gain at two different biases for three different samples with η set to 0.14, 0.20 and 0.28. a) Gain at 50 mV/period. b) Gain at 58 mV/period. Here an almost linear increase in gain can be seen.

that especially $\eta = 20$ is much different from $\eta = 14$. It seems that the value of the constant strongly influences the lifetime of the states and which transitions yields gain or not, as discussed above in the linear response section. In order to calibrate the η parameter we have to have some kind of demands. First, the structure should be lasing at these low temperatures. Burghoff *et al.* [6] states that their structure lases at a wide range of millivolts and that they have gainclamping at 18 cm^{-1} due to internal losses in their cavity, so we need gain above 18 to simulate the gain that they see in the experiment. They also report a peak current at 420 A/cm^2 . These conditions applied to figure 17b and 16 suggest that $\eta = 20$ is currently the best choice of the three options compared.

3.4 Linear response of a QCL

In order to evaluate the properties of a QCL, calculations must take into account the *linear response* of the system. This will describe the interplay of the internal dynamics of the system with an external electromagnetic field. In our nomenclature, the internal dynamics is governed by the bias and how the system responds to it in terms of scattering and current through the structure. This *stationary behavior* can be calculated by including only terms of $h = 0$ in the harmonic expansion of the time dependant part of the Hamiltonian shown in eq. (31). Increasing h to 1 will allow interactions with an external oscillating electromagnetic field and will give the linear response. As the cryostat temperature was 33 K in the experiment, a higher lattice temperature is expected as the laser structure is heated under operation. Therefore the simulations are carried out at a lattice temperature of 77 K.

3.4.1 Linear response calculations

Using the Non Equilibrium Green's Function Theory (NEGFT) a number of simulations were carried out in order to characterize the structure using the model presented above. At first, I-V characteristics were simulated. The current is simulated with an external bias only, i.e. without an electric field oscillating in time. This corresponds to the $h = 0$ case and is shown in fig. 18. This can be directly compared to the experimental results of fig. 12a on page 31 taking into account that the voltage is simply 175 times the bias per period. The overall shape of the

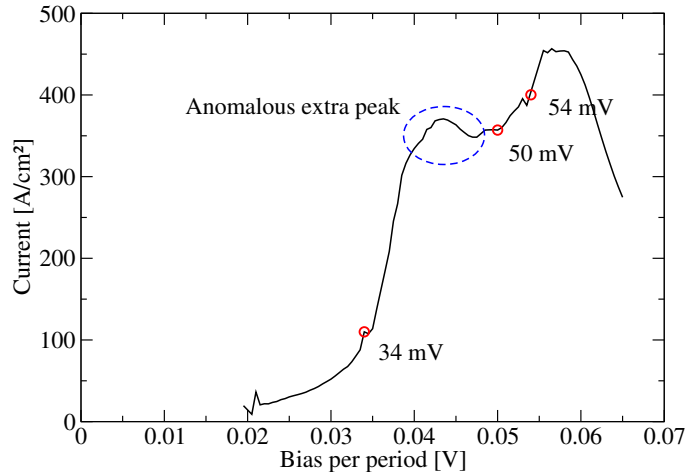


Figure 18: Simulated current response to external bias on the system. The points corresponding to about the same points as were examined in the reference [6] are marked with red circles. The currents at these points is 110 A cm^{-2} (34 mV), 357 A cm^{-2} (50 mV) and 400 A cm^{-2} (54 mV).

curve matches the green curve of fig. 12a very well, and looking at the current we find that it is reproduced with high accuracy. Location compared to the bias is not exactly right, as we find that the point at 54 mV per period corresponds to 9.5 V, which is too low. This could be an effect of an unnoted bias drop in the contacts in the experiment of [6]. We also note a first peak in current around 43 mV per period

that do not show up in fig. 12a, instead we would expect a linear behavior up to the operating point. The reason for a first current peak could be that the model we are using does not take into account electron-electron scattering. We will postpone this discussion to the later section 3.8 on page 55. The points in fig. 18 marked with red circles are the ones that are to be investigated further, as they are good candidates for being roughly the same points as investigated in [6]. Next the results

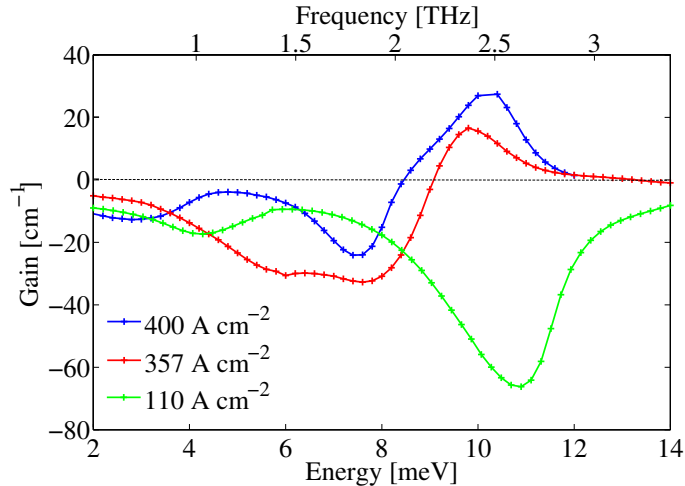


Figure 19: Simulated linear response at three different current points indicated in fig. 18. Units also in THz, for easier comparison to the reference results in fig. 13 on page 31.

from a linear response calculation are presented in fig. 19. Again the overall shape is in good match with the experimental results. In the higher frequency region the main features are well reproduced, the peaks and dips of the curves are at roughly the same positions, just as in fig. 13 on page 31 and the height of the blue curve peak is also double the red curve peak as expected, and the green curve has a shape that is almost identical to its measured counterpart.

In the lower frequency region our results show a more complex structure for the curves of 357 and 400 A/cm² than the experimental results, in which the data have been fitted to two Lorentzian profiles. The red as well as the blue curve from the simulations show two absorption peaks and not one as approximated in fig 13, page 31. There is a discrepancy of the peak for the maximum gain at 10 meV at the operating point of 400 A/cm². While the reference [6] has a peak in the gain at a bit over 9 meV (2.2 THz) we have it at 10 meV. This arises an important question; can we somehow explain this discrepancy? In order to understand these results and explain why the experimental data is not fully reproduced a number of investigations were made.

3.4.2 Identifying energy transitions

In the gain spectra from the simulations it is often hard to evaluate which transitions contribute and are visible. There are five active states, and one could naively expect transitions among all of them. A number of factors are important in determining the strength of each transition. The occupations of the different states, the dipole matrix

elements for each transition and more things as we shall see. To try to understand an example, we will look closer at the low current curve (green) from fig 19, at a bias of 34 mV per period. In this case the shape of the curve resembles the one seen in the experiment (fig. 13 page 31) although the dips are not at the right positions. In

	1	2	3'	4'	5'
ρ (%)	89.3	3.2	5.5	1.4	0.6
1	0	9.2	0.55	5.39	13.89
2	-	0	8.65	3.81	4.69
3'	-	-	0	4.84	13.34
4'	-	-	-	0	8.5

Table 3: The absolute value of transition energies for the states shown, together with the occupations of the levels in percent. Units in meV.

order to evaluate which transitions correspond to each dip we need to know, among other things, the difference in energy between the relevant states. At this bias, the Wannier-Stark states will look as in figure 20 where the square of the wavefunctions are plotted. In the plot we see that the transitions with the lowest energies, below the optical phonon region ($E_{\text{optical phonon}} \approx 37\text{meV}$) that separates the groups of states, are the transition among levels 1 (red), 2 (green), 3' (turquoise), 4' (pink) and 5' (orange), where the prime means that the state are of the next neighboring period. At this low bias of 34 mV/period – operating bias is at 54-56 mV/period

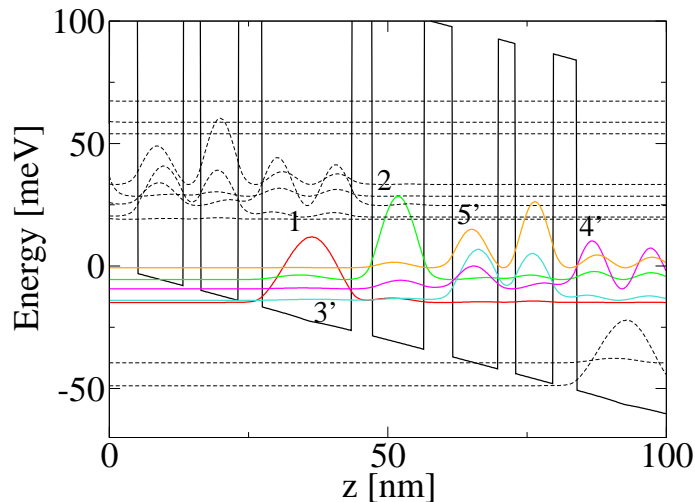


Figure 20: Wannier-Stark states in the central period. Here we zoom in to see the groundstate and the closest higher states.

– most of the electrons, in this particular case it is 87%, are resident in the lowest state 1. The first assumption would then be that the strongest absorption peaks should be from state 1 to the other states above. The calculations show a strong absorption peak at 10 meV in fig. 19, and by comparing with table 3 this matches with $1 \rightarrow 2$, but this is the only state 1 transitions that corresponds well to fig. 19. The others do not match in energy. We also calculate a small absorption peak at

4 meV and the transition $1 \rightarrow 4'$, which could be assumed to be this lower one, is of higher energy so this can't be the transition that is visible. The question is which transition corresponds to the low absorption peak and why the other ones are not showing up, especially 1 to 4'? And why is there about 1 meV mismatch for the calculated high energy absorption peak compared to the experimental data in fig. 13 on page 31?

3.4.3 Densities and Spectral functions & Red and Blue shift of transitions

Depending on whether we look at absorption or gain the transition energies might be a bit shifted. This is because in reality, the energy states are not discrete but smeared out as they have a finite lifetime (we are describing a dynamic process). This broadens the levels, allowing for blur and red shifts of the transitions between the states. Recall the spectral function, which we interpret as a density of state function in both k and energy.

$$A(\mathbf{k}, \omega) = i [\mathbf{G}^{ret}(\mathbf{k}, \omega) - \mathbf{G}^{adv}(\mathbf{k}, \omega)] \quad (52)$$

In our system, we have a quantized z -direction (growth direction) so the spectral function is a periodic function in z as well as in energy (shifted with $eF_{dc}d$ for each period), where \mathbf{k} holds the x - and y -dependence. From the NEGFT code we extract the spectral function as the retarded and advanced Green's functions are known, at a specific k . As shown in fig. 21 lines at the energy maxima can be found, and

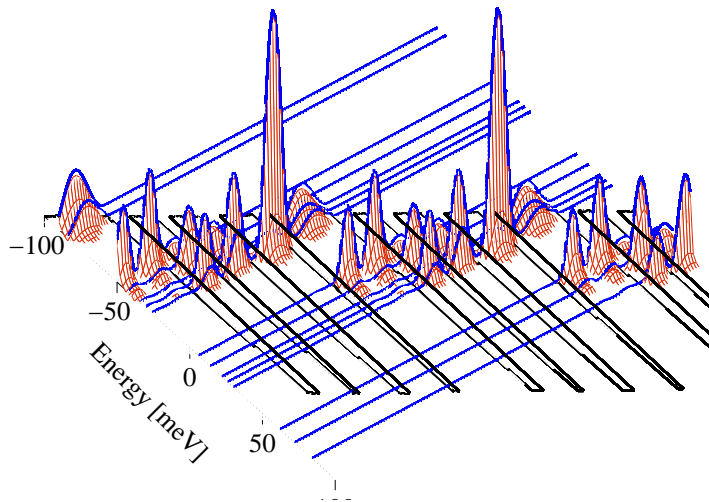


Figure 21: The spectral function at $k = 0$ shown for almost 3 periods together with the band structure. At each energy maxima on line is selected.

they can be used as an alternative representation of the states. They better match the energy resolved carrier densities extracted from the calculation as shown in fig. 22, as the comparison in fig. 23 shows. The calculated values for the WS states and the spectral function maxima is shown in table 4. Another useful property of the spectral function is that it can be used to refine the predictions of the transition energies. Transitions between states will most likely be from where there are many

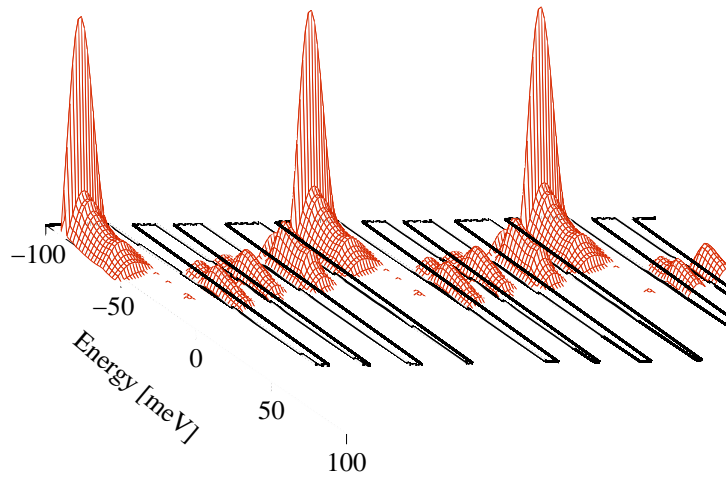
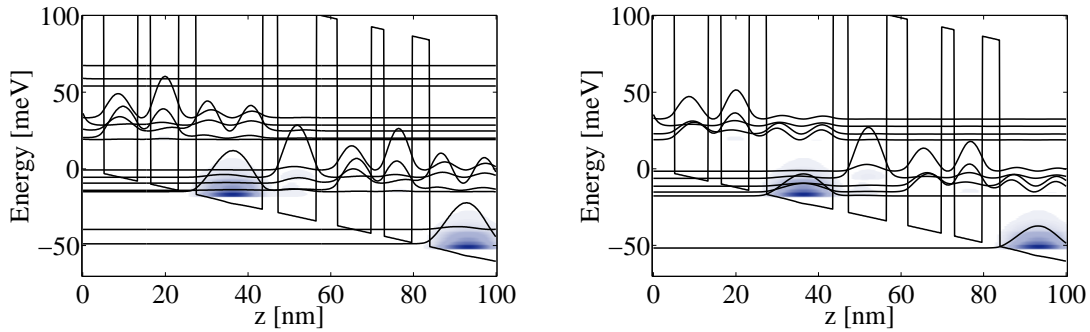


Figure 22: Here the electron density is shown for 34 mV/period together with the band structure. It is this plot that is used to get to fig. 23a.



(a) The electron densities shown together with the Wannier-Stark states.

(b) The electron densities shown together with the spectral function at the peaks in energy as shown in fig. 21.

Figure 23: Comparison between Wannier-Stark states and spectral function with respect to the energy resolved carrier density.

Level	1	2	3'	4'	5'
WS	-14.9	-14.0	-9.3	-5.5	-0.7
$\mathbf{A}(\mathbf{k}, E)$	-17.7	-6.2	-15.2	-11.35	-1.6

Table 4: Compared energy levels for WS states and spectral function.

electrons, to where there are few electrons, as shown in fig. 24. In other words, the strongest transition will be from a maxima of the density function, (example in fig. 22) to a maxima of the spectral function. In a thermalized situation, the lower states will be filled first, and the low energy states will be filled, and the high energy states empty. This induces a red shift for emission transitions (which will give gain) and a blue shift for absorption transitions [27].

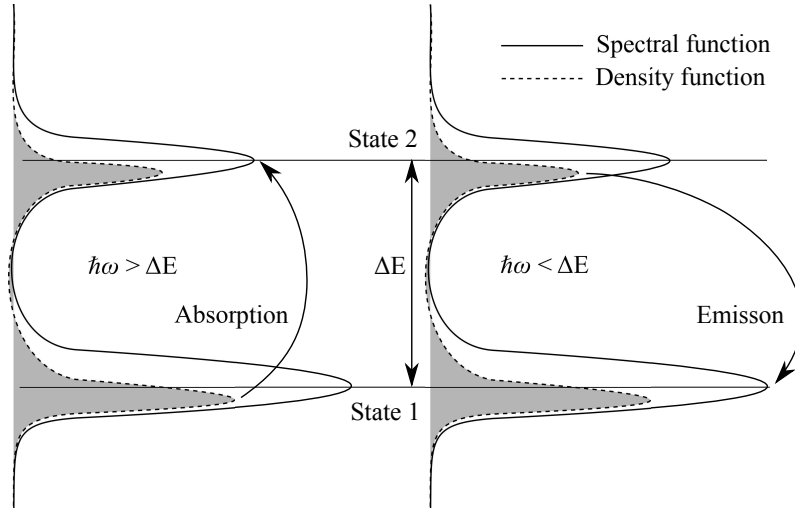


Figure 24: Sketch showing how transitions get blue and red shifted. The discrete states are shown with some broadening. As the most probable transition is from the energy with the most electron to the energy where there are as maximum of free states, transition energies will vary.

3.4.4 Modal gain calculations

In this section we will try to interpret the results from the simulations – not the experimental results. We look again at the calculated linear response at a bias of 34 mV per period, shown as the green curve in fig. 19 on page 36. To reduce the complexity of the gain calculations, we will use a simpler expression (eq. (42) derived above on page 24 following [8]) for modal gain in the following discussion:

$$G(\omega) = \frac{e^2 |z_{lo,up}|^2 \omega (n_{up} - n_{low})}{2dc\epsilon_0 \sqrt{\epsilon_r}} \frac{\Gamma}{(E_{up} - E_{lo} - \hbar\omega)^2 + \Gamma^2/4} \quad (53)$$

where $z_{lo,up}$ is the dipole matrix element, $n_{up/lo}$ is the densities of the upper and lower levels, d is the period of the structure, Γ is a broadening i.e. the full width maxima which is dependent of the lifetime of the state considered, ω is the frequency and E is the energies for the different states. From the equation it is clear that we need the transition energy, the matrix element and the difference in occupation to calculate the gain/absorption for each transition. The transition energies are presented in table 3 on page 37. From this information it is clear that only the transition $1 \rightarrow 2$ can account for the transition at 10 meV, with approximately 1 meV redshift. The only energy we find which would fit the low energy transition with approximately 1 meV redshift is the transition from $4' \rightarrow 2$.

Now we also need to look at the matrix elements of the different transitions. In the expression for gain given in eq. (53) we see that the matrix element enters the formula squared, so it is indeed vital for the discussion. They are here calculated from the Wannier-Stark functions shown as scaled squares in fig. 20 on page 37 and presented in table 5. From this information it is clear that the transition from $4' \rightarrow 2$ can indeed be the transition responsible for the low absorption in figure 19 on 36. But a quick look at the densities of each state shows that state 2 with 3.2% of the electrons is actually more occupied than state $4'$ with only 1.4%, strongly reducing

	1	2	3'	4'	5'
1	-	3.3	5.25	3.6	0.15
2	-	-	0.075	11.0	7.6
3'	-	-	-	7.2	1.8
4'	-	-	-	-	5.9

Table 5: Matrix elements for transitions between the different states of interest. Units in nm and signs dropped.

that probability (as state 2 is of higher energy than 4'). So we can conclude that, as the transition $3' \rightarrow 2$ is ruled out by the infinitesimal matrix element, that the interesting processes must be $1 \rightarrow 2$, $1 \rightarrow 4'$ and $3' \rightarrow 4'$.

As a final part we will also look at the energies of the spectral function to see if we find any energy corrections to the states of interest, as suggested in fig. 24. The spectral function shows where the states are but not to which degree they are filled, so it is not affected by the distribution function as the total density function would be. We take the energy difference by looking at where the densities are the highest, from where the most transitions will probably occur, and then assume that the absorption will be the most when the transition is to the maximum of the corresponding spectral function, as there will be most states at that energy. We find $\Delta E_{12} = 11$ meV, $\Delta E_{14'} = 6.1$ meV and $\Delta E_{3'4'} = 4.1$ meV. An estimate using eq. (53) gives that state 1 to 2 should give highest absorption followed by 1 to 4' and then 3' to 4'. The other transitions are of lower orders of magnitude. As an explanation of the result, this is good but still not accurate. The energies of the transitions are closely matched, but still it cannot be explained *which* transitions that show up.

3.4.5 Rediagonalizing the density matrix

In a further attempt to understand what is happening in our simulations, a new base of eigenfunctions instead of the Wannier-Stark functions is established. During the calculations the Wannier basis is used, with the strong advantage that it is independent of the external bias. After the calculation the Wannier-Stark basis is easily calculated which is a better representation of the true basis (and energy eigenstates). As can be seen in fig. 23a on page 39 there is a small mismatch in energy, and we do not understand which transitions in the gain simulations that are important. The question whether there is a better set of basis functions arises.

One possibility is to use the eigenfunctions of the density matrix, as done in [28]. $\mathbf{G}^<(E)$ is an energy dependent density matrix containing the occupations and correlations of the basis states. The $\mathbf{G}^<(E)$ matrices extracted for each energy point in the structure are diagonalized and the calculated energy dependent eigenvalues are seen in figure 25. For each peak in occupation we take our new basis functions as linear combinations of the Wannier states, given by the eigenvector corresponding to the the chosen eigenvalue. To calculate the dipole matrix element we have to proceed with care, since we now have a basis diagonal with respect to occupations. Instead of using equation (42) on page 24 or 40 we take a couple steps back and

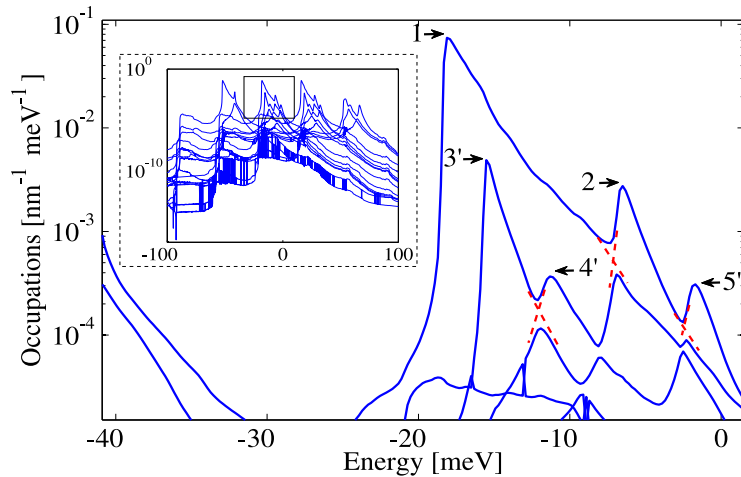


Figure 25: Energy dependent eigenvalues of $\mathbf{G}^<(E)$. Different level crossings can be seen, and one of the peaks are excluded from the analysis due to the fact that it is just a crossing. We identify the correspondence to the old states by the occupations. The new states are taken as the eigenfunctions of the eigenvalue at the different local maxima of the branches.

	1	2	3'	4'	5'
1	-	5.3	0.09	0.20	0.5
2	-	-	1.0	9.2	9.1
3'	-	-	-	14.0	1.0
4'	-	-	-	-	26.0

Table 6: Matrix elements squared for transitions between the different states of interest. Calculated by the p_z operator expectation values in the new basis of eigenfunctions to the chosen eigenvalues of $\mathbf{G}^<(E)$, at a bias of 34 mV/period.

instead use the dipole matrix element due to the p_z operator, as shown in eqs. (47). This places the ω in the denominator instead and generally changes what constants we have. To compare transitions, we will use

$$G(\omega) \propto \frac{|\langle \varphi_{up} | p_z | \varphi_{lo} \rangle|^2 (n_{up} - n_{lo})}{\omega} \cdot \text{Lorentzian distr.} \quad (54)$$

Calculated matrix elements squared in arbitrary units are shown in table 6. With these dipole matrix elements we can calculate the relative strengths of the different absorptions with the help of equation (54), and they are shown in table 7. For comparison we associate a Gaussian shaped absorption centered at each transition energy and given the calculated relative strength, and this demonstrates how the calculated absorption almost generates the results of the *full* simulations in figure 19 on page 36. It is a crude approximation to use the same width for every transition, as their lifetimes are different, but it is still illustrative. Comparing fig. 26 to the green curve in fig. 19 on page 36, both at 34 mV/period, we see that a good understanding of the calculations is now reached. The eigenstates of the density

	1	2	3'	4'	5'
1	-	12	0.87	0.78	0.79
2	-	-	0.08	1.0	1.3
3'	-	-	-	3.9	0.09
4'	-	-	-	-	0.43

Table 7: Absorption strength of the transitions in arbitrary units. Calculated with equation (54), at a constant bias of 34 mV/period.

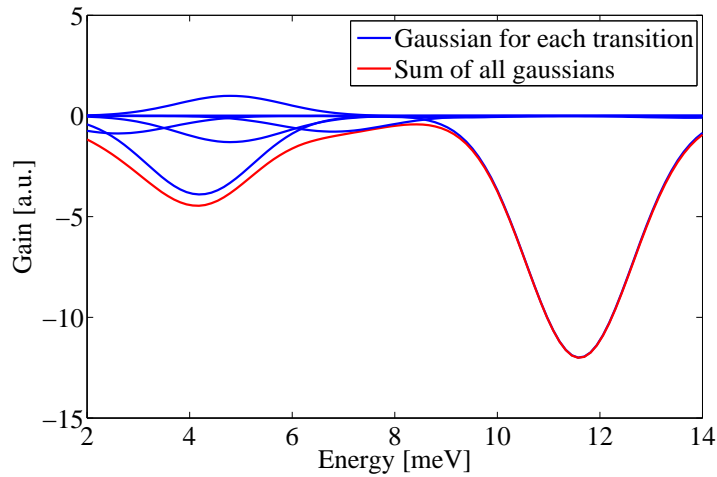


Figure 26: Every transition energy is given a Gaussian with a FWHM of 2.5 meV (blue) and the summed result is also shown (red). These calculations are done at a bias of 34 mV/period and this result can then directly be compared with the green curve in fig. 19.

matrix are a good help in interpreting the results produces when we simulate the response of the sample. One could argue that these states should have been used from the beginning, as they have the good physical properties. On the contrary, these states are not localized in the way the Wannier states are but periodic in z . Using them would give us no information about where in the structure we are.

3.5 Nonlinear response calculations

At a low intensity external field the system can be described with a linear response model as described in the sections above. This gives a detailed picture and can be understood as probing the system with a fine instrument, not perturbing the system too much by the measurement. At a high intensity field however, this is no longer a fine probing, but a large perturbation of the system dynamics. It can no longer be understood by a linear response model when the perturbation is in the same order of magnitude as the direct bias of the heterostructure. A successful QCL is a high

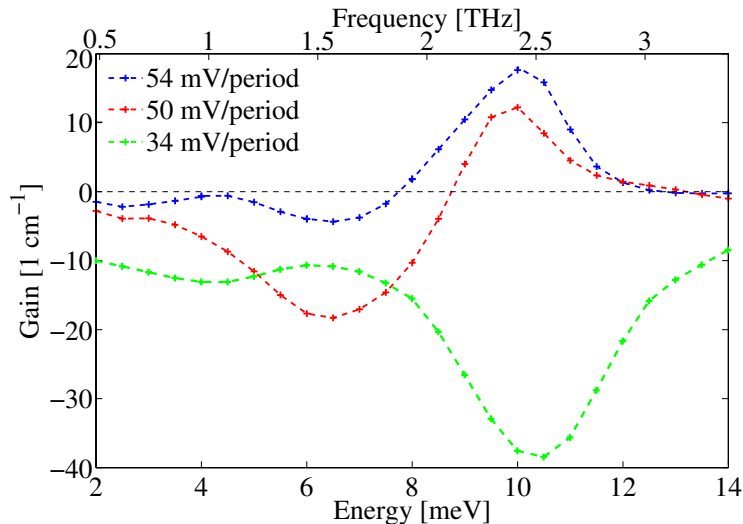


Figure 27: Nonlinear response calculations at the same bias points as in the linear response case shown in figure 19. The intensity of the external field is $eF_{ac}d = 0.006$, which is 11% of the DC field of 0.054 V/period.

intensity QCL, so it is of great interest to model the high intensity response - the nonlinear response. To do this higher order harmonics of the light field are included, the parameter h in the equation is varied to both 2 and 3. This will in principle allow for higher order excitations by the field. In figure 27 nonlinear response calculations are shown. The points selected are the same bias points as for the calculations for linear response, in order to be able to compare them correctly. As the intensities are high here, they will effect the transport properties of the system. We know from before that a good QCL has mechanisms for population inversion, and a high intensity field at the right energy will effectively destroy this inversion, as the electrons are quickly deexcited by stimulated emission, enhancing transport i.e. current. In figure 28 this can clearly be seen, we go from a current of about 400 A cm^{-2} to a much higher current at 470 A cm^{-2} by raising the intensity from $eF_{ac}d = 0.001$ to $eF_{ac}d = 0.006$.

In the calculations a number of different intensities and bias points were used in order to see if a good agreement with experiment could be achieved. One can note that the current at the intensity chosen in figure 27 is higher than the experimental results. Although this is not that far off, it could depend on different parameters and other approximations. The key point in examining the nonlinear response for many different bias points and intensities is to relate them to the data of our reference,

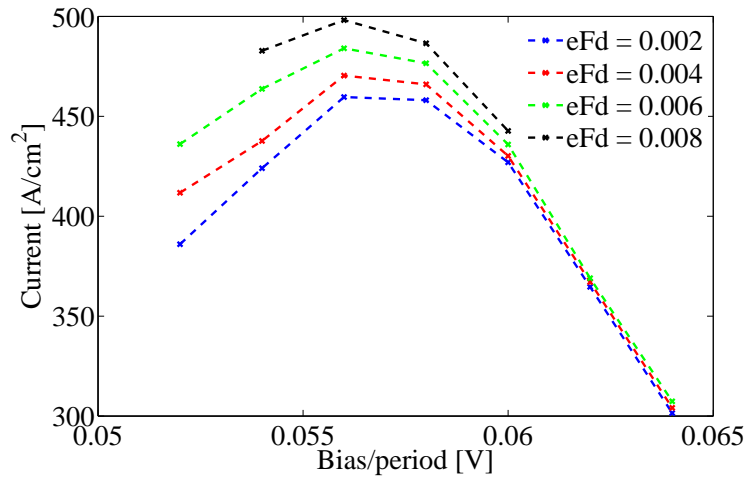


Figure 28: The current at the chosen operating point at different intensities. Note that the peak is not shifted with higher intensities.

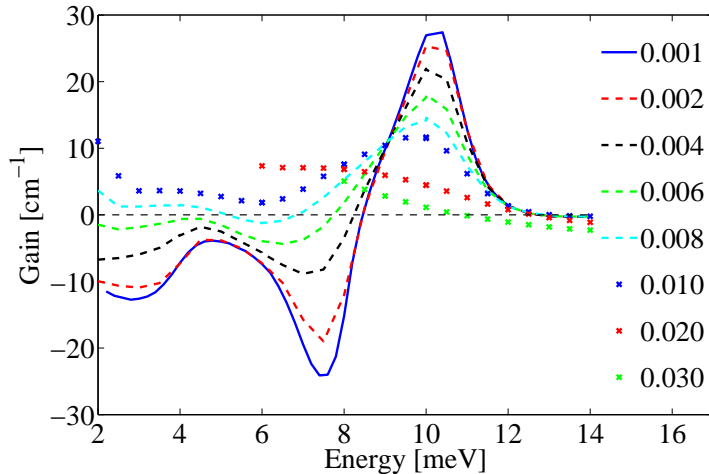


Figure 29: Absorption plot at 54 mV/period at various intensities. Note that fewer points are available at higher intensities due to convergence issues. The main behavior of the gain peak is a linear decrease with intensity.

presented in figures 12a,12b,13 on page 31, in order to see if nonlinear calculations are more closely related to the experimental data. By showing that the high intensity response corresponds better to the one observed in the reference experiment [6], it is likely that the measurements they made were actually not linear response measurement but highly nonlinear. Comparing figure 19 on page 36 and figure 27 we see that the features are smoothed as we go to higher intensity. This can also be studied in figure 29. It is no longer three independent peaks or dips but instead they almost float together, more resembling the reference data. This can be the reason that Burghoff *et. al* [6] fit a double Lorentzian to their data, as seen in fig. 13 on page 31, whereas in our linear response case, fig. 19 on page 36, this would not have worked at all. Other things to notice are that the dips are now approaching the same values as the experiment, but are still about one meV off. We still have

lasing at a too high frequency. In the following sections we will try to address all of these issues.

The peaks and dips in the plots are also decreasing in magnitude with increasing field strength, also shown in figure 29. In the same figure we also find information about what we can interpret as a system crash. This is when the oscillating field and the direct field are approaching the same strength. We see that at a intensity of $eF_{ac}d = 0.030$ the gain spectra is almost flat: the inversion is totally destroyed. The spectra also shows a number of strange features when approaching frequencies close to zero. Comparing higher intensities to the one with $eF_{ac}d = 0.001$ we see that there is an increase in gain at these small frequencies. Here the NEGFT code issues a warning that the value of nh is too low. In order to see if there is any physics behind this behavior, it will be necessary to study these points in more detail in order to find out what is happening here. This will be examined in one of the following subsections.

3.5.1 Gain clamping

In figure 12a on page 31 the gain of the QCL studied in [6] is shown as a function of bias. After reaching lasing threshold the gain *clamps* at 18 per cm, it can't go over that value. Then it is said that the *internal losses* of the lasing cavity is 18 per cm. This is what has to be overcome in order to get this structure to lase. If the gain is under 18, the intensity enhancement will be lost in the cavity. If the gain is higher than 18, then the intensity will go up dramatically, as now the losses of the cavity are overcome, and the surplus intensity is used to start the lasing process of stimulated emission. This starts a chain reaction that will eventually destroy the inversion. When the gain goes below 18 again, the surplus gain is gone, and the lasing stops. This is why one can see a stabilization around the level of the cavity losses. How is this related to our nonlinear response calculations? By looking at the calculated gain as a function of both external field intensity and bias, a similar thing to gain clamping can be achieved. For each bias point for which gain has been calculated for a range of intensities, the intensity which corresponds to a gain of 18 per cm can be found. This is the intensity to which to real laser would clamp. At different biases, this gain of 18 per cm will correspond to different intensities, thus we can establish a measure of the optical power that is extracted. Then a plot of optical power versus bias can be created. Looking at figure 30, a number of intensities can be selected at the line which indicates a gain of 18 per cm. As we have seen before, the decrease in gain is almost linear (figure 29), allowing for interpolations to find the correct gain values. The values found are presented in table 8 below, and the data is used to calculate the intensity (which is basically the

mV	50	52	54	56
$eF_{ac}d$ [eV]	0	0.0046	.0060	0.0064
I [mW/ μm^2]	0	0.0290	0.0494	0.0562

Table 8: The field strength and optical intensity at a gain of 18 cm^{-1} for the different bias points examined

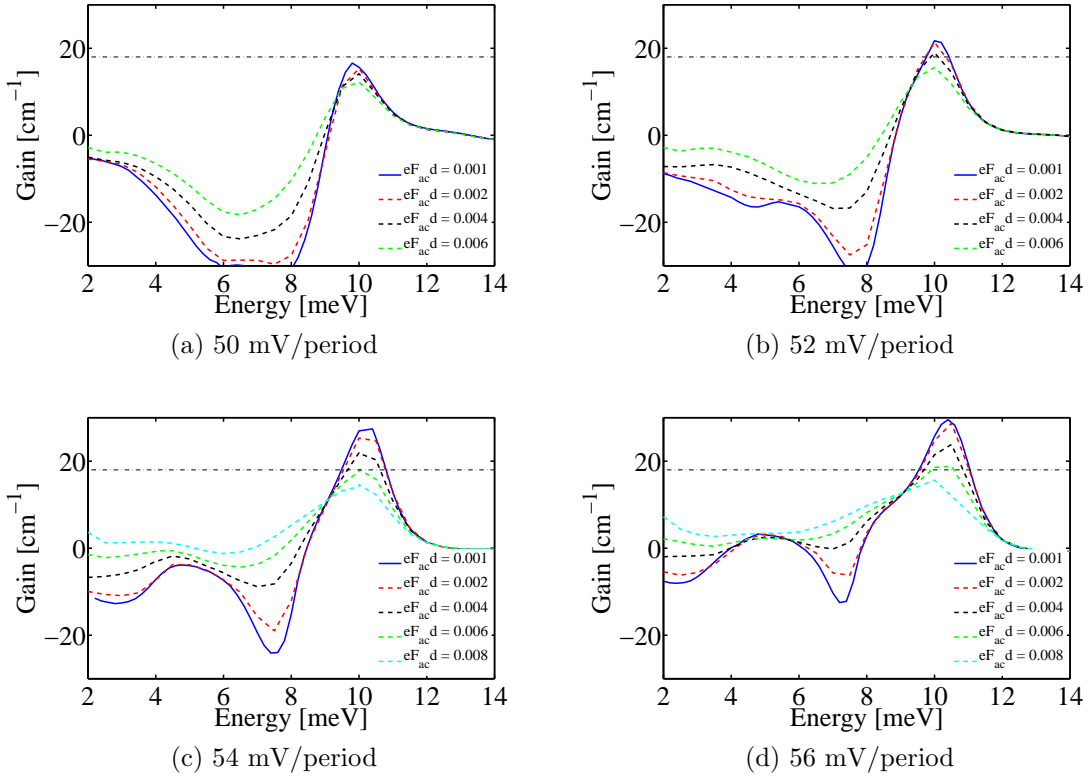


Figure 30: Plots of gain spectrum at different biases and different intensities. Included in each plot is a line indicating gain of 18 per cm (dash-dot). The value at this point, taken by linear interpolation, is then used to calculate the optical power at that point.

square of the field strength), and this is shown in figure 31. In the study by Burghoff *et al.* [6] they describe how the pump laser pulse was fed into the QCL. The facet was of the size $10 \times 80 \mu\text{m}$ onto which a 125 mW pulse with a spot size of $20 \mu\text{m}$ was focused. Note that the spot size was double the size of the QCL. A quick estimate with the Poynting vector shows that

$$I = (eF_{ac}d)^2 \frac{nc\epsilon_0}{2e^2d^2}$$

$$\Rightarrow eF_{ac}d = \sqrt{I \cdot \frac{2d^2}{nc\epsilon_0}}, \quad (55)$$

where $eF_{ac}d$ is in units eV, n is the refractive index, in this case $n = 3.3$. The pulse will cover only a fourth of the facet, and with Fresnel losses we estimate that at most 15% of the light is coupled into the structure. The average intensity will then be $125 \text{ mW}/800 \mu\text{m}^2$ and by eq. (55) we get

$$eF_{ac}d = 0.004 \text{ eV}$$

and that shows that we are in the right region with the intensity measurements, as the most interesting calculations are in fact done at intensities of 0.004-0.008 eV.

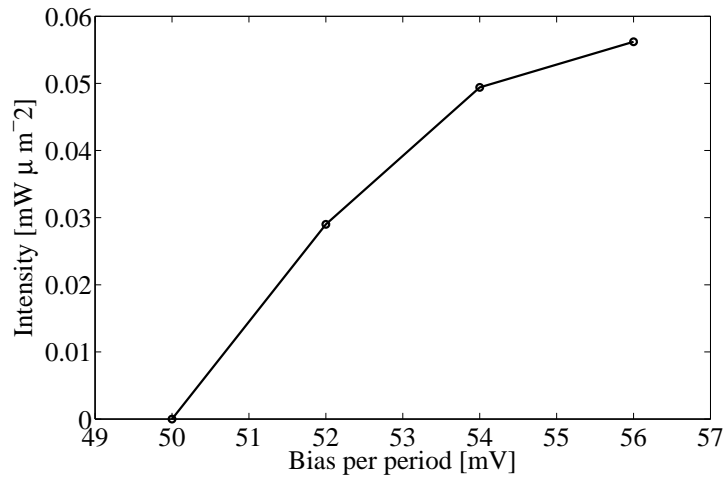


Figure 31: The intensity, or optical power, is plotted in arbitrary units. This can be compared to figure 12a on page 31.

3.5.2 Convergence studies

Figure 32 shows a plot that is similar to figure 29 on page 45 but zoomed in focusing on a region between 0 and 10 meV. In the plot data is presented from a number of simulations in the very low frequency part of the spectra. When doing calculations at low frequency or high intensity an estimate is used in order to evaluate if enough Fourier components are included, i.e. if h is high enough. The simulations shown in fig. 32 were done in order to see if this calculated estimate that constitutes the warning is accurate.

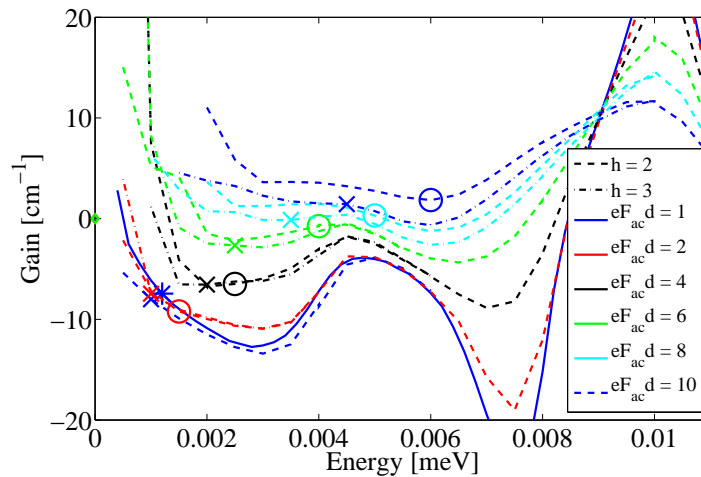


Figure 32: Basically the same plot as fig 29 on page 45 but with more data. Units in the legend for the field strengths $eF_{ac}d$ are in meV. The circles (crosses) show the last point in the set for $h = 2$ ($h = 3$) without warning.

In the plot there are points calculated with $h = 2$ and 3. It is also shown where warnings for low values of h are issued. For $h = 2$ there are circles at the last point we estimate to be good, and in the same way crosses for $h = 3$. Note that the

warnings come at lower energies as h is increased from 2 to 3, so by raising h we estimate that the results will be better in these regions.

As $h = 3$ is the highest value used, we must assume that these calculations are the most accurate. The interesting points in the data sets then are the ones at higher energy than the crosses, and their relation to the corresponding points for $h = 2$. At lower energies it is hard to draw any conclusions, but it seems that going from $h = 2$ to 3 reduces the divergent behavior at all intensities.

Going to low frequencies is the same as going to low energies. If the field strength is very high, meaning a high intensity with a lot of energy for the system to absorb or to create stimulated emission, going to low energies we need to allow for multiple excitations. Only allowing for single ($h = 1$) or even double excitations ($h = 2$), does not seem to be enough. Consequently, when approaching zero energy radiation, we would need harmonics to infinite order. This is the reason for the main trend in fig. 32 as the warnings are at higher energies for higher intensities, where we also see a large mismatch between $h = 2$ (dashed) and $h = 3$ (dash-dot). Looking at each intensity measurement in fig. 32:

For 1 meV (blue) the plot is not entirely consistent, as calculations for $h = 1$ and $h = 2$ is plotted, but the warnings are in good agreement, and the calculations at higher energies are in good match.

At 2 meV (red) both the circle and cross seem to be placed correct.

At 4 meV (black) the warnings seem to be correct.

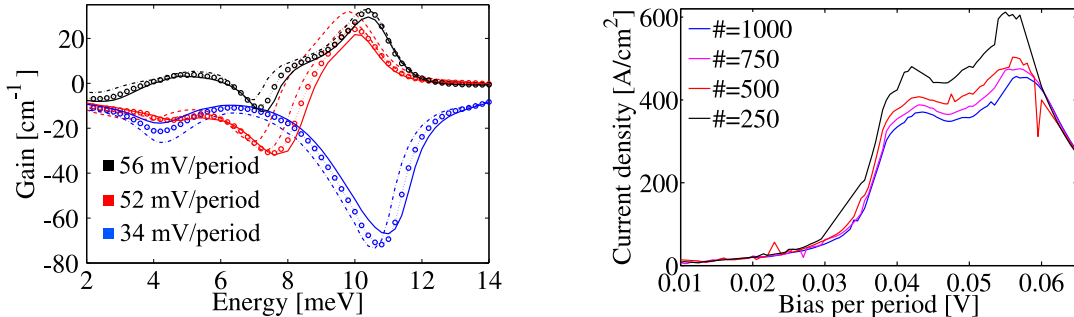
At 6 meV (green) we see that the circle is really the last point that is in good agreement with the data set for $h = 3$.

At 8 and 10 meV (cyan)(blue) however, there seem to be some problems. The circle warnings seem to be issued a bit late as it is in fact at 10 meV that the calculations for $h = 2$ and $h = 3$ match. The mismatch is larger at 10 meV intensity.

In summary, the estimate used is highly accurate at most intensities, around 10% of the constant bias over the structure. The 4 meV data set (black) gives a good example of this. At higher intensities at 15% and more of the constant bias, the results and warnings becomes inconsistent, and the $h = 2$ warnings cannot be considered to be accurate.

3.6 Energy shifted peaks in gain spectra

In figure 33a a gain simulation at a bias of 50 mV/period is shown, where the number of k -points used in the simulation has been varied. In each simulation the discretization is however the same, so in fact, it is the maximum k that is changed. There is a inconsistency here that must be addressed, as the physical result should not be dependent on how many k -points that are used. It has been



(a) Gain spectra changes when varying the number of k -points used. Solid lines means 1000 k -points, dots with circles 750 k -points, dotted-dashed 500 k -points (and dashed 250 k -points but only for 52 mV/period).

(b) A increase in current is seen when decreasing number of k -points.

Figure 33: Showing effects of varying number of k -points in grid

suggested by A. Wacker² that using a k -independent scattering matrix element as discussed in section 2.3.1 might cause problems. This might make the integral in phase space (k -space) divergent with an x^{-1} behavior, for large k . Looking at the most dominant part of for example the retarded self energy, i.e. the diagonal elements of the expression in the self consistent Born approximation in an isotropic space in x and y ,

$$\Sigma_{\alpha\alpha}^{ret}(E, E_k) = \int dE'_k X_{\alpha\alpha}^{ret}(E, E'_k) G_{\alpha\alpha}^{ret}(E, E'_k)$$

the approximation of a k -independent $X_{\alpha\alpha}^{ret}$ means that we can move it outside, and this will then give an integral in E'_k of $G_{\alpha\alpha}^{ret}$, which can be approximated by [13]

$$\begin{aligned} G_{\alpha\alpha}^{ret}(E, E'_k) &\approx \frac{1}{E - E_\alpha - E'_k - i\Gamma/2} \\ &= \frac{E - E_\alpha - E'_k}{(E - E_\alpha - E'_k)^2 + \Gamma^2/4} - i \frac{\Gamma/2}{(E - E_\alpha - E'_k)^2 + \Gamma^2/4}. \end{aligned}$$

Here the E_α is included to account for the period index, and Γ is a broadening. Integrating this quantity is fine in the second term, but the first term behaves as $1/(E - E_\alpha - E'_k)$ for large E'_k which is indeed divergent. As it does not approach

²Personal communication, December 2011

zero sufficiently fast, it might give a artificial contribution to the self energies

The way the energy space and the k -space is discretized is shown in figure 34.

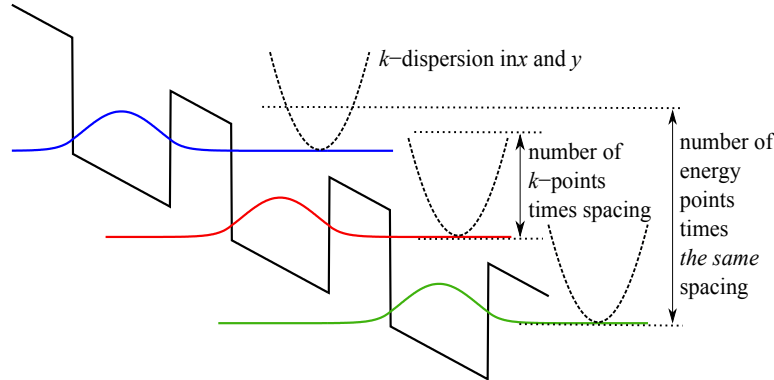


Figure 34: The two different grids are shown and how they relate to each other. The k -parabola is drawn in the z -direction for clarity but is in reality in the x - and y -direction, where the bands are parabolic. Remember that the *discretization in energy* is the same for both grids.

The number of points in the energy grid is chosen by the user when the code is run. A high number i.e. high finesse means good accuracy but at the same time longer computing times. Spanning from the lowest energy possible to the highest, the grid is established with the number of points chosen (the maximum energy is taken as the energy level of the highest laying state included, plus two thermal energies at chosen temperature and the Fermi energy of the band). At the same time as a grid is taken, a spacing between the points is calculated. The same spacing is then used for the grid in k -space starting at zero and with a choseable number of k -points. This number is varied in figure 33. Now figure 35 shows the distribution function

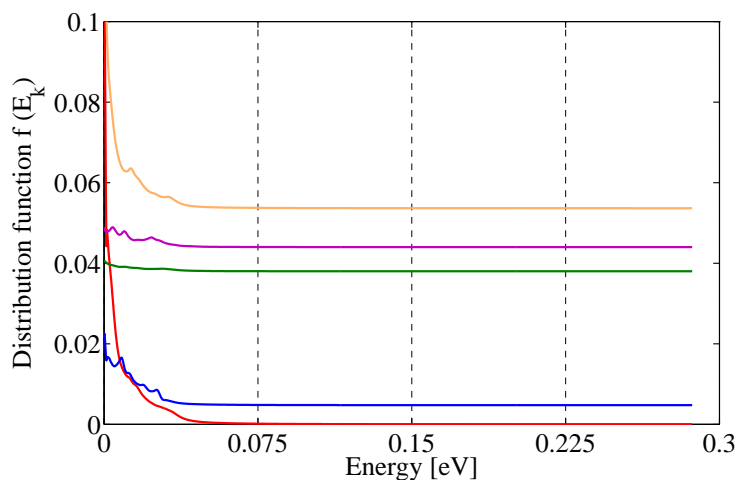


Figure 35: Showing the distribution function for the first five states in a period at 55 mV bias/period. The number of k -points are 1000.

among the k -states. The electrons are mostly at the low energies, temperature is as

in the other example around 77 K. The unoccupied k -states are not unimportant, the higher lying states allows for electron scattering into a state with a high energy and subsequent relaxation down to normal occupation energies, as well as electron excitation and through that scattering into another higher energy state. But by looking at figure 35, it should be possible to truncate k -space somewhere without changing the physics too much. Scattering to high lying k -states should not be that probable. Figure 33 shows the result of different such truncations. As the result differs much even when only high lying empty k -values are taken away, the effect of the constant matrix element seems to play a big role when simulating this structure. We can see that the current increases a bit as we decrease the number of k -points. This can be a scattering effect, but why would the gain and absorption peaks get shifted in energy (they are also shifted in magnitude, which is related to different currents) when changing this? This leads to the conclusion that the k -independent scattering matrix elements in the self energy must be treated carefully when simulating this structure, and that the peaks and dips in the gain/absorption spectrum might be artificially shifted.

Looking at the blur curves in fig. 33a corresponding to a bias of 34 mV/period. The order of the peak shift at 11 meV is about 0.5 meV to lower energies. At the same time, the peak shift at 4 meV is smaller, but in the other direction. We note that comparing the experimental results in fig. 13 on page 31 to the response calculated in fig. 27 on page 44 we would get closer to the experiment if the left peak moved right, and if the right peak moved left. This is alone no argument for it to be true, but looking at the red curve we see that both peaks, at 8 meV and at 10 meV, get shifted to lower energies as we consider fewer k -points (or limit the highest k). Decreasing the k -points down to a fourth of the energy points (dashed red in fig. 33a) also increases the order of the shift to 1 meV. A shift like this is of the same magnitude as the discrepancies we see when we compare the calculations to the measurements, so they can indeed be relevant in interpreting our simulations. A truncation at one fourth of the energy points does sound a bit drastic, but studying fig. 35 we at least do not cut away any occupied states.

3.7 Integrated absorption of a QCL

The integrated absorption is estimated by summing over all possible transitions with corresponding strength and also over all frequencies. Here we look at the integrated absorption from all intersubband transition, and by the Thomas-Reiche-Kuhn sum rule [1][2] it can be expressed as a constant only dependent on the average carrier density n_{av} and of course the usual material constants, as discussed above in section 2.5. Eq. (49), page 27:

$$\int_0^{\infty} d\omega \alpha_{intersubband}(\omega) = n_{av} \frac{\pi e^2}{2m_c c \sqrt{\epsilon} \epsilon_0}$$

This should be preserved even with a bias over the structure present. The average carrier density is calculated by taking the sheet density divided by the period length, the mass is taken to be the GaAs effective mass as the electrons reside in the wells most of the time and the ϵ is taken to be in the low frequency limit for GaAs which then would be equal to 13. For the structure presented in [6] the integrated absorption is found to be

$$n_{av} \frac{\pi e^2}{2m_c c \sqrt{\epsilon} \epsilon_0} = 2.4107 \text{ eV cm}^{-1}$$

The average carrier density can then be found out using the sheet density of carriers in the sample, a quantity that is often experimentally well known from the growth process and also experimentally. In our case the sheet density is used as an input parameter, and it is the number density of electrons in a period of the QCL, and is then a areal or sheet density. To get the conventional average density we then divide it with the period length. One approximation made in the calculations is that the electron is in the wells and not in the barrier although we know that this is not entirely true and is also contradicted by the functionality of a QCL. As the effective mass is higher in the barriers having a percentage of Al, using the effective mass for the well might lead to higher theoretical value. The simulation was done

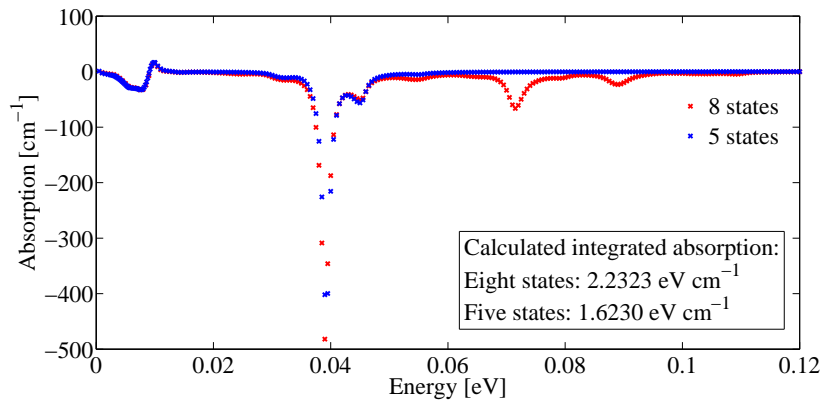


Figure 36: Simulated data points for absorption for a biased QCL structure at 50 mV. Data cut at 120 meV.

with both five and eight transporting states taken into account and the results can

be seen in figure 36. As can be seen from the results eight states almost reproduce our theoretical result but not in all total. Possible reasons can be, as stated just above, that the the effective mass is underestimated, but it can also be so, following the reasoning that eight states produced much more absorption than the five states, that increasing the number of states available in the transport calculations would give more possible transitions and thus more absorption at the higher frequencies. Most likely the error is a combination of these factors.

In [25] integrated absorption was considered for a superlattice using the same model as in this work. The estimated error they give is 0.3 eV, and compared to our error of 0.2 eV this is well within their error margins.

Calculating backwards from the measured integrated absorption yields a correction of 16.5% in the effective mass towards the barrier mass, meaning that if this is the only effect causing the higher theoretical value the electrons should be in total 16.5% in the barriers. This number seems too big at first glimpse, but if there are more errors, this number would decrease a bit.

3.8 Phenomenological inclusion of electron-electron scattering

When the stationary behavior of the QCL studied in this work was presented in fig. 18 on page 35 a small peak in current could be seen before operating bias was reached. The same curve is shown again in fig. 37 (full blue line). Comparing with experimental results, figs. 12a and 12b on page 31, this small peak is not seen, and might be unphysical. One possibility is that it is an effect of leaving out electron-electron scattering from the model. A way to mimic electron-electron

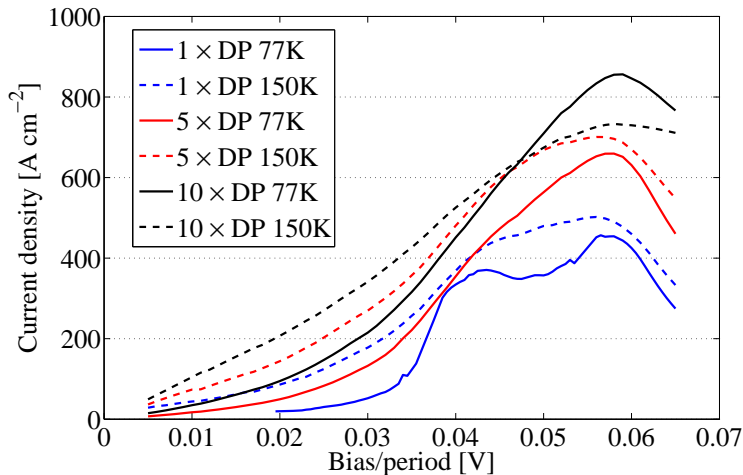


Figure 37: Shows the IV characteristics of the structure at different temperatures and values of the deformation potentials.

scattering, suggested by A. Wacker¹ and implemented together with M. Lindskog, is to artificially increase the *deformation potential* in the system, making the otherwise weak [21] acoustic phonon scattering stronger. This was tried out and the results is seen in fig. 37 for five and ten times the ordinary deformation potential (DP). The plot shows how a higher DP increases scattering and produces more current, as we would expect since we have artificially increased scattering, but we also see how the current-peak at ≈ 55 mV per period dominates already at 5 DP for 77 K (red full line).

A DP of 10 times the original value makes too large of an impact on the system dynamics and dramatically influences the lifetimes and widths of the states. Such a high value would disturb the system too much, but half the value, 5 times the original potential, is a more reasonable value to get a quick feeling for how electron-electron scattering would affect the system.

In fig. 38 we can see how the carrier distribution changes with DP and temperature. When increasing DP, as well as temperature, the electrons become more thermalized, and more spread in the k -states. This is an effect that we think electron-electron scattering would have on the system. In the same figures the thermal behavior can also be studied, as we can see that thermal backfilling from state 1 to state 3 and

¹Personal communication, autumn 2011

4 is possible at 150 K. This shows how the laser becomes less efficient with higher temperatures.

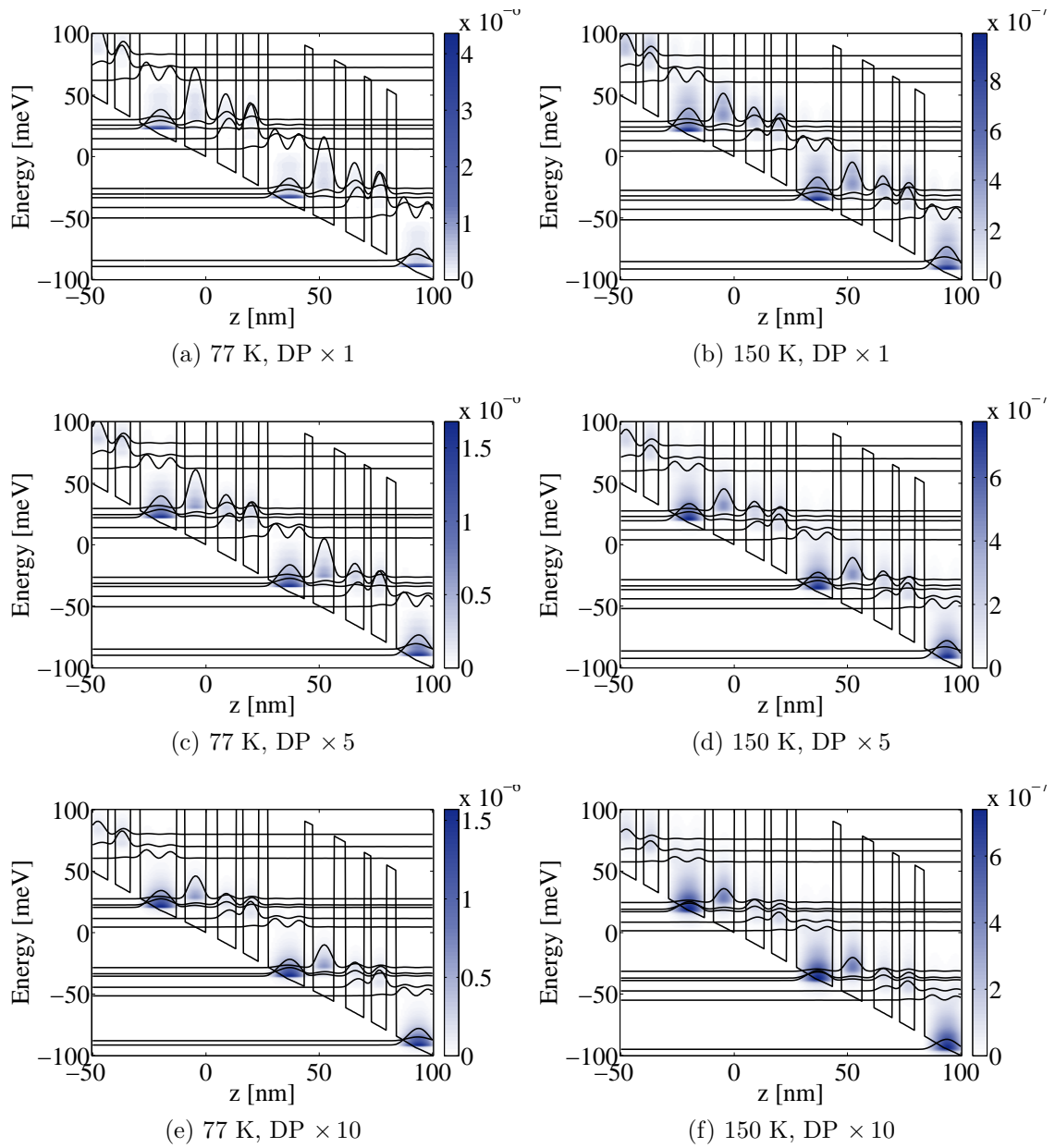


Figure 38: Densities at the given temperatures and deformation potentials.

4 Conclusion

In this work, the structure presented in [6] has been investigated thoroughly in a theoretical study. The model is formulated in the nonequilibrium Green's function picture, with specific considerations in the self energies. Using this model, many aspects of this QCL have been considered, as interface roughness scattering, integrated absorption, k -space truncation and convergence issues at high electromagnetic field intensity. Most important are the dynamic properties of the QCL at operating conditions. At these operating conditions the system is strongly perturbed by the laser field created by the population inversion, and big changes in the system compared to the linear response behavior are expected.

We show that the model is capable of reproducing these experimental results to high extent. The I-V characteristics are simulated in good accordance to the experiment, as well as the linear and nonlinear response of the system to high intensity electromagnetic fields. The simulations of the system at high intensity was made by including higher order Fourier components of the response function in the nonequilibrium Green's function picture, and by doing so, we find that the measurements made in the experiment [6] do not correspond to linear but rather nonlinear response.

References

- [1] W. Kuhn, *Z. Phys. A* **33**, 408 (1925).
- [2] F. Reiche and W. Thomas, *Z. Phys. A* **34**, 510 (1925).
- [3] M. Rochat and et. al., *Applied Physics Letters* **81**, 1015 (2002).
- [4] B. S. Williams, *Nature Photonics* **1**, 517 (2007).
- [5] F. Capasso, *Optical Engineering* **49**, 111102 (2010).
- [6] D. Burghoff, T.-Y. Kao, D. Ban, A. W. M. Lee, Q. Hu, and J. Reno, *Applied Physics Letters* **98**, 061112 (2011).
- [7] S. Kumar, Q. Hu, and J. L. Reno, *Applied Physics Letters* **94**, 131105 (2009).
- [8] A. Wacker, in *Nonlinear Laser Dynamics: From Quantum Dots to Cryptography*, edited by K. Ldge (Wiley-VCH, Weinheim, Germany, 2011), Chap. Quantum Cascade Laser: An Emerging Technology.
- [9] J. Faist, F. Capasso, C. Sirtori, D. L. Sivco, J. N. Baillargeona, A. L. Hutchinson, S. G. Chu, and A. Y. Cho, *Appl. Phys. Lett* **68**, 3680 (1996).
- [10] G. Mahan, *Many-Particle Physics* (Kluwer Academic/Plenum Publishers, New York, 1981).
- [11] A. L. Fetter and J. D. Walecka, *Quantum theory of many-particle systems* (Dover publications, Inc., Mineola, New York, 1971).
- [12] M. E. Peskin and D. V. Schroeder, in *An introduction to quantum field theory*, edited by D. Pines (Westview Press, Boulder, Colorado, 1995).
- [13] H. Haug and A.-P. Jauho, in *Quantum kinetics in transport and optics of semiconductors*, edited by D.-I. H. K. Lotsch (Springer-Verlag, Berlin Heidelberg, 1996).
- [14] J. Rammer and H. Smith, *Rev. Mod. Phys.* **58**, 323 (1986).
- [15] D. C. Langreth, in *Linear and Non Linear Electron Transport in Solids*, edited by J. T. Devreese and V. E. van Doren (Plenum Press, New York, 1976).
- [16] L. Kadanoff and G. Baym, *Quantum Statistical Mechanics* (Benjamin, New York, 1962).
- [17] L. P. Keldysh, *Sov. Phys* **20**, 1018 (1965).
- [18] A. Wacker, *NEGFT-program Manual*.
- [19] T. Brandes, *Phys. Rev. B* **56**, 1213 (1997).
- [20] A. Wacker, *Phys. Rep* **357**, (2002).

- [21] R. Nelander, Ph.D. thesis, Lund University, 2009.
- [22] S.-C. Lee and A. Wacker, Phys. Rev. B **66**, 245314 (2002).
- [23] A. Wacker, R. Nelander, and C. Weber, in *Proceedings of SPIE Vol. 7230*, edited by A. A. Belyanin and P. M. Snowton (SPIE, Bellingham, WA, 2009), Vol. 7230, 7230 1A.
- [24] J. J. Sakurai, in *Modern Quantum Mechanics, Revised Edition*, edited by S. F. Tuan (Addison-Wesley Publishing Company, Inc., 1994).
- [25] A. Wacker, G. Bastard, F. Carosella, R. Ferreira, and E. Dupont, Phys. Rev. B **84**, 205319 (2011).
- [26] B. Williams, S. Kumar, Q. Hu, and J. Reno, Electron. Lett. **40**, 431 (2004).
- [27] A. Wacker, Nature Physics **3**, 298 (2007).
- [28] S.-C. Lee, F. Banit, M. Woerner, and A. Wacker, Phys. Rev. B **73**, 245320 (2006).